

**AD-A265 492**



①

THESIS/DISSERTATION  
XXXXXXXXXX

Determination of the Robustness of Passive Microwave  
Measurements and Derivative Parameters for use in  
Precipitation Discrimination Over Land

John S. Shattuck, Captain

AFIT Student Attending: Florida State University

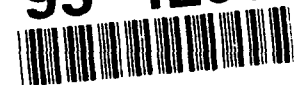
AFIT/CI/CIA-92-121

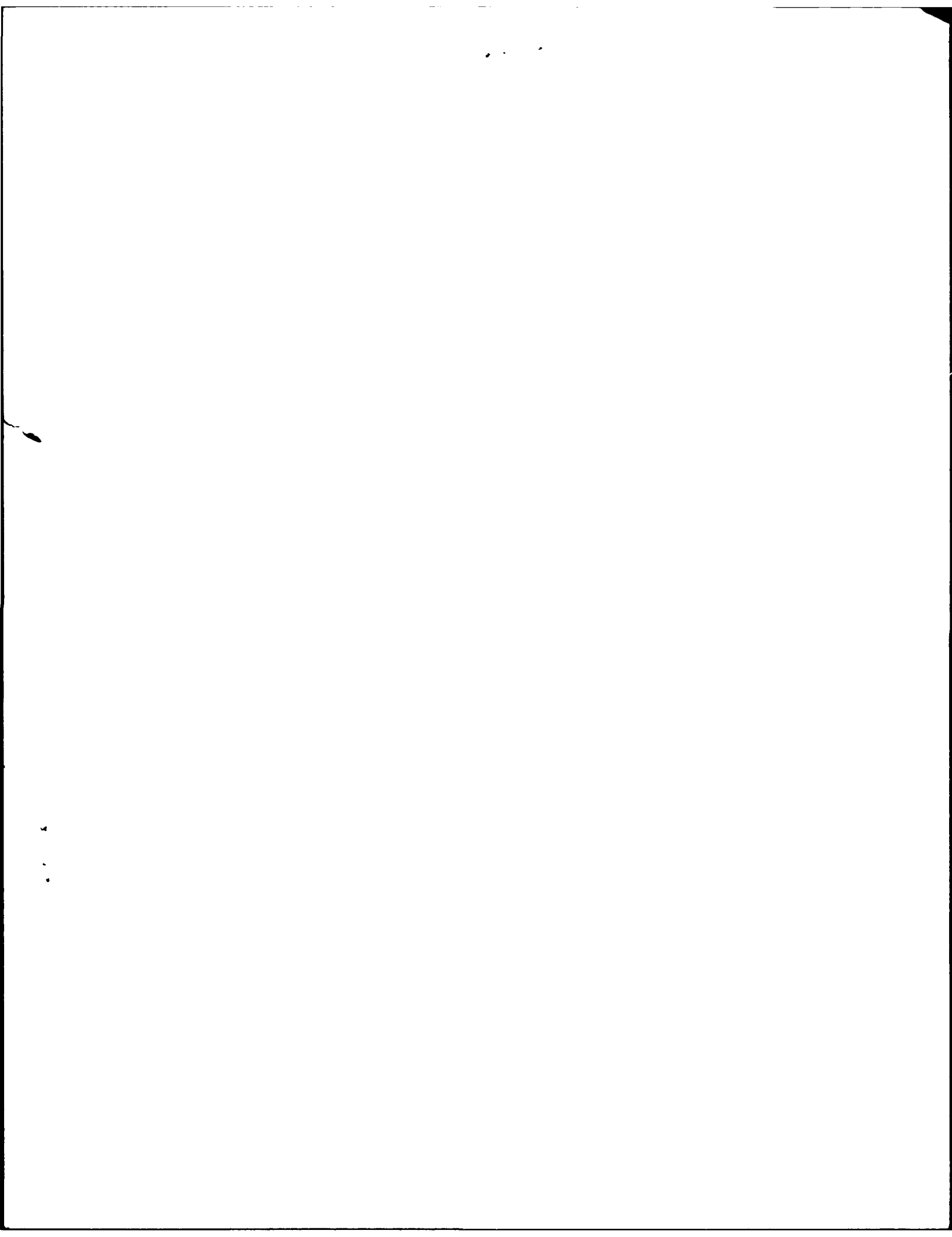
AFIT/CI  
Wright-Patterson AFB OH 45433-6583

Approved for Public Release IAW 190-1  
Distribution Unlimited  
ERNEST A. HAYGOOD, Captain, USAF  
Executive Officer

DTIC  
SELECTE  
JUN 07 1993  
S B D

**93-12639**





THE FLORIDA STATE UNIVERSITY  
COLLEGE OF ARTS AND SCIENCES

DETERMINATION OF THE ROBUSTNESS OF PASSIVE MICROWAVE  
MEASUREMENTS AND DERIVATIVE PARAMETERS FOR USE IN  
PRECIPITATION DISCRIMINATION OVER LAND

By

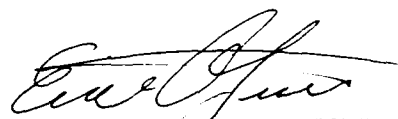
JOHN S. SHATTUCK

A Thesis submitted to the  
Department of Meteorology  
in partial fulfillment of the  
requirements for the degree of  
Master of Science

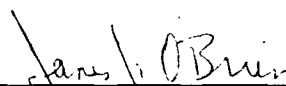
Degree Awarded:

Fall Semester, 1992

The members of the Committee approve the Thesis of John S. Shattuck  
defended on July 23, 1992.



Eric A. Smith  
Professor Directing Thesis



James J. O'Brien  
Committee Member



Kevin A. Kloesel  
Committee Member

DTIC QUALITY INSPECTED 2

Accession For	
NTIS GRA&I	<input checked="checked" type="checkbox"/>
DTIC TAB	<input type="checkbox"/>
Unannounced	<input type="checkbox"/>
Justification	
By	
Distribution/	
Availability Codes	
Dist	Avail and/or Special
A-1	

## Acknowledgements

I wish to thank the members of my committee, James O'Brien and Kevin Kloessel, for taking the time to review and offer suggestions regarding my research. I would also like to thank my major professor for having a great deal of patience with me and for the critical examination and advice concerning my studies and research. A very special thanks is due to Jim Merritt and his invaluable computer support with programming and graphics which saved me countless, stressful hours at the lab.

I would like to thank Barbara Benton and Karen Wolfe of the office staff for their assistance and support. Last, but not least, I thank my wife Connie for having the patience with me during the past two years (most of the time).

This research has been supported by NASA Grant NAG-991 and NSF Grant ATM-8812411.

## Table of Contents

<b>List of Tables</b>	vii
<b>List of Figures</b>	ix
<b>Abstract</b>	xii
<b>1 Introduction</b>	1
1.1 Background	1
1.2 Motivation	9
<b>2 Methodology</b>	12
2.1 Probability Distribution Function Formation	12
2.2 Quality Control Procedures	15
2.3 Robustness of Individual Parameters	21
2.4 Robustness of Multi-parameter Combinations.	22
2.5 Testing of Single and Multi-parameter Models on Independent Data Sets	23
<b>3 Data Sources</b>	24
3.1 Indian Subdivisional Rainfall	24
3.2 SSM/I Passive Microwave Measurements	26
3.3 INSAT Infrared Measurements	26

<b>4 Analysis of Microwave and Infrared Histograms</b>	<b>27</b>
4.1 Robustness Analysis of Individual Parameters	27
4.1.1 Properties of the Microwave Probability Distribution Functions	27
4.1.2 Properties of the Infrared Probability Distribution Functions	45
4.1.3 Properties of the Microwave Cumulative Distribution Function	48
4.2 Robustness of Multi-parameter Combinations	50
4.2.1 Model Building with Microwave Parameters	52
4.2.2 Model Building without 85V GHz Parameters	55
4.2.3 Model Building with Microwave and IR Parameters	58
<b>5 Validation Tests</b>	<b>63</b>
5.1 1987 Tests	63
5.2 1989 Tests	69
<b>6 Rainfall Accumulation</b>	<b>75</b>
6.1 Monsoon Features	75
6.2 Space and Time Averages	77
6.2.1 1988 Accumulations	77
6.2.2 1987 Accumulations	83
6.2.3 1989 Accumulations	83
<b>7 Summary and Conclusions</b>	<b>91</b>

References	95
Biographical Sketch	98



## List of Tables

Table	Caption	Page
1.1:	SSM/I Channel footprint dimensions.	6
1.2:	Definition of microwave and IR parameters.	11
3.1:	Weeks used in 1987, 1988, and 1989 for this study.	25
4.1:	Correlation coefficients and RMS errors for the mean of the 1988 microwave PDFs.	30
4.2:	Correlation coefficients and RMS errors for the standard deviation of the 1988 microwave PDFs.	43
4.3:	Correlation coefficients and RMS errors for the mean of the 1988 IR PDFs	47
4.4:	Correlation coefficients for the slope factor of the 1988 microwave CDFs.	51
4.5:	Correlation coefficients for the intercept factor of the 1988 microwave CDFs.	51
4.6:	Parameters used in optimal regression model along with correlation coefficients and RMS errors at each step.	54
4.7:	Mean + standard deviation regression model parameters with correlation coefficients and RMS errors.	57
4.8:	WO85V multi-parameter regression model parameters correlation coefficients and RMS errors.	58
4.9:	IR-microwave optimal regression model parameters with the correlation coefficients and RMS errors.	62

5.1:	Parameter correlation coefficients and RMS errors for 1987.	65
5.2:	Parameters used in independent 1987 regression model along with correlation coefficients.	68
5.3	Parameter correlation coefficients and RMS errors for 1989.	71
5.4:	Parameters used in independent 1989 regression model along with correlation coefficients.	73

## List of Figures

Figure Caption	Page
2.1 Indian subdivisions used for weekly rainfall totals.	13
2.2 19VE probability distribution functions for 20 weeks in 1988 for Konkan and Goa. Low $T_B$ peak represents pixels containing ocean contamination.	16
2.3 19VE probability distribution functions for 20 weeks in 1988 for Madhya Maharashtra illustrating typical non-contaminated 19 GHz probability distribution functions.	17
2.4 37VE probability distribution functions for 20 weeks in 1988 for Jammu and Kashmir illustrating affects of snow on 37 GHz probability distribution functions.	19
2.5 37VE probability distribution functions for 20 weeks in 1988 for East Rajasthan illustrating typical 37 GHz probability distribution functions.	20
4.1 Correlation coefficient vs. microwave parameter. Mean of morning and evening microwave Probability Distribution Functions (1988).	29
4.2 Scatter diagrams for a) $19V_M$ , b) $19V_E$ , c) $19H_M$ , and d) $19H_E$ .	31
4.3 Scatter diagrams for a) $22V_M$ and b) $22V_E$ .	33
4.4 Scatter diagrams for a) $37V_M$ , b) $37V_E$ , c) $37H_M$ , and d) $37H_E$ .	34
4.5 Scatter diagrams for a) $85V_M$ , b) $85V_E$ , c) $85H_M$ , and d) $85H_E$ .	36

4.6	Scatter diagrams for a) $19U_M$ , b) $19U_E$ , c) $37U_M$ , d) $37U_E$ , e) $85U_M$ , and f) $85U_E$ .	37
4.7	Scatter diagrams for a) $19PCT_M$ , b) $19PCT_E$ , c) $37PCT_M$ , d) $37PCT_E$ , e) $85PCT_M$ , and f) $85PCT_E$ .	39
4.8	Scatter diagrams for a) $19DIF_M$ , b) $19DIF_E$ , c) $37DIF_M$ , d) $37DIF_E$ , e) $85DIF_M$ , and f) $85DIF_E$ .	41
4.9	Correlation coefficients for the mean + standard deviation of the morning and evening microwave PDFs (1988).	44
4.10	Difference between evening and morning correlation coefficients for the mean + standard deviation of the PDFs(1988).	46
4.11	Diurnal cycle of cloudiness as seen in the fluctuations of IR correlation coefficients.	49
4.12	Regression Model Correlation Function (RMCF) for optimal multi-parameter model based upon the mean of the 1988 PDFs.	53
4.13	RMCF for optimal multi-parameter model based upon the mean + standard deviation of the 1988 PDFs.	56
4.14	RMCF of optimal IR-microwave model based upon the mean of the 1988 PDFs.	61
5.1	Correlation coefficients of the mean of the 1987 morning and evening PDFs.	64
5.2	RMCFs of the Optimal 1988 microwave multi-parameter model applied to 1987 data and the independent 1987 multi-parameter model.	67
5.3	Correlation coefficients of the mean of the 1989 morning and evening PDFs.	70
5.4	RMCFs of the WO85V 1988 microwave multi-parameter model applied to 1989 data and the independent 1989 multi-parameter model.	72

6.1	Measured and model estimated 1988 subdivsional weekly rainfall and the difference between the measured and estimated data.	76
6.2	Measured and model estimated 1987 subdivsional weekly rainfall and the difference between the measured and estimated data.	78
6.3	Measured and model estimated 1989 subdivsional weekly rainfall and the difference between the measured and estimated data.	79
6.4	1988 continental weekly rainfall accumulation weighted by subdivision size.	80
6.5	1988 subdivsional seasonal rainfall accumulation weighted by subdivision size.	81
6.6	1988 subdivsional seasonal rainfall accumulation map.	82
6.7	1987 continental weekly rainfall accumulation weighted by subdivision size.	84
6.8	1987 subdivsional seasonal rainfall accumulation weighted by subdivision size.	85
6.9	1987 subdivsional seasonal rainfall accumulation map.	86
6.10	1989 continental weekly rainfall accumulation weighted by subdivision size.	87
6.11	1989 subdivsional seasonal rainfall accumulation weighted by subdivision size.	89
6.12	1989 subdivsional seasonal rainfall accumulation map.	90

## ABSTRACT

In this study, a large set of microwave and infrared parameters, derived from the Special Sensor Microwave/Imager (SSM/I) and the Indian Geosynchronous Satellite (INSAT), are examined to qualitatively determine how much contrast exists between raining and non-raining conditions over land. The precipitation regime of the Indian summer monsoon was chosen for the evaluation testbed. Each of the microwave parameters contain measurements which were enhanced, through a deconvolution technique, to match the spatial resolution of the 85 GHz channel (15 x 13 km). The microwave and infrared measurements are grouped into Probability Distribution Functions (PDFs) and Cumulative Distribution Functions (CDFs) containing one week of measurements for each parameter and time of satellite measurement within a Indian subdivision. The mean and standard deviation of each PDF and the slope and intercept factors of each CDF are tested for robustness against weekly subdivisional raingage data.

The robustness of each of the parameter variables are determined by an evaluation of their correlation coefficient obtained through a linear least squares fit. Once the robustness of each parameter variable is quantified in terms of its relationship to rainfall, a statistical rainfall estimation algorithm is generated on a training data set from 1988. The algorithm is then validated on independent data

sets from two different years. The algorithm achieves correlation coefficients of -0.75 and -0.80 in 1987 and 1988, respectively. The algorithm performance suffers in 1989 due to the lack of useable measurements from parameters containing the 85V channel.

# CHAPTER 1

## Introduction

### 1.1 Background

Since the advent of satellite technology, atmospheric scientists have sought to monitor global weather conditions from space, including the distribution of rainfall. Early satellite precipitation retrieval techniques relied on visible and infrared data which related cloud parameters such as cloud-top-temperature, albedo, or fractional cover to rainrate or volumetric rainfall. These techniques could only give an indirect estimate of precipitation at best, and it was not until the introduction of microwave sensors that direct estimates of rainfall from satellite platforms were possible.

Physically-based passive microwave rainfall retrieval methods fall into three classes, emission-, scattering-, and inversion-based. Emission-based retrievals make use of the low frequencies (e.g. 19 GHz) and are primarily useful over oceanic regions. At microwave frequencies, even though water is a strong dielectric, the ocean appears cold due to the low emissivity of its surface ( $\sim 0.5$ ) caused by only a portion of the wave being transmitted across the relatively flat ocean-atmosphere interface with the remainder reflected back into the ocean. In contrast, raindrops have a high emissivity, due to the dimensions of the emitted waves being equal or exceeding that of the drops, thus allowing the internally generated waves to pass through the drop surface.



Therefore rain appears warm against the radiometrically cool ocean background. Land surfaces, on the other hand, have generally high microwave emissivities and thus appear warm. This decreases the contrast between rain and the land. As a result, emission methods do not work as well over continental regions.

Scattering-based retrievals utilize higher frequencies such as 37 or 85-90 GHz which are quite sensitive to the amount of ice suspended within the atmosphere. A depressed brightness temperature ( $T_B$ ) arising from scattering by frozen hydrometers can then be used to estimate the amount of precipitation falling out of a cloud because of the inherent correlations between ice concentrations and rainrates. Inversion methods attempt to determine the vertical hydrometer structure of the atmosphere using forward radiative transfer (RTE) models to adjust initial guess hydrometeor profile information until the calculated  $T_B$ s are in agreement with the measured  $T_B$ s. Once the vertical rain water profile is known, a surface rainrate can be calculated. Of these three physically-based retrievals, the emission- and scattering-based methods are useful in evaluating the performance of the microwave parameters examined in this study. The inversion method is not applicable because information concerning the vertical hydrometeor structure, on the time and space scales used in the study, are not available.

Wilheit, et al. (1977) developed an emission-based retrieval scheme using a successive order of scattering RTE model incorporating a Marshall-Palmer raindrop distribution and fixed thermodynamic and cloud water parameters, to retrieve rainfall over oceanic regions. Tests of the scheme utilizing Nimbus 5 Electrically Scanning Microwave Radiometer (ESMR-5) 19 GHz data showed that satellite estimates could be related to radar derived rainrates within a factor of two. Of major significance was that the theoretical calculations revealed a strong non-linear relationship between rainrate

and 19 GHz  $T_B$ s emerging from the top-of-atmosphere (TOA). The non-linearity results in two significantly different rainrates for the same  $T_B$ . Wilheit's paper demonstrated, for the first time, that rainrates could be determined by microwave radiometry based upon a physically-based model over oceanic regions. More recent emission-based algorithms such as those of Smith and Mugnai (1988) and Hinton et al. (1992), have simply refined various aspects of the Wilheit algorithm.

Microwave retrieval methods over land have been more difficult to formulate due to the lack of contrast between the rainfall and the radiometrically 'hot' land background. The problem is compounded by the varying emissivities of different components of the surface (i.e. vegetation, bare rock, sand, etc.), varying soil moisture, and temperature within a radiometer field-of-view (FOV). Schmugge (1983) showed that soil moisture has a strong inverse effect on land surface emissivity since it increases the dielectric constant of the soil which in turn results in lower emissivity. Thus, for the lower microwave frequencies in which the surface contributes to the TOA signal in the presence of rain, varying soil moisture poses a difficult boundary condition problem.

Early theoretical work using both 19 and 37 GHz ESMR-5 and ESMR-6 measurements suggested that rainfall over land could be detected at 37 GHz but not at 19 GHz due to incomplete beam filling by either rain or land caused by the large FOVs at 19 GHz (Savage and Weinman, 1975; Weinman and Guetter, 1977). In addition, they suggested that discrimination between rainfall, and wet or dry land would be possible by taking advantage of the degree of polarization at 37 GHz. At the intermediate frequencies, rainfall and dry land are essentially unpolarized with land often having higher  $T_B$ s than rain. On the other hand wetted land surfaces can be significantly polarized and thus present another type of signal contrast to rain. Variations in the degree of polarization at 37 GHz can also be related to land surface characteristics and

their temporal variability (Choudhury, 1989). His study shows that polarization decreases with increased vegetation and surface roughness, while polarization increases with increasing soil moisture and FOVs contaminated by open water such as lakes or rivers. Therefore, the degree of polarization can be used as a signature which discriminates between rainfall and various characteristics of the underlying surface.

Observational work by Rodgers et al. (1977) concluded that rain detection over dry land is difficult if the surface thermodynamic temperatures are less than  $15^{\circ}$  C. This is because as the surface thermodynamic temperature decreases, the  $T_B$  of the surface also decreases which in turn leads to a lack of contrast between rainfall and the land surface. However, if surface temperatures exceed  $15^{\circ}$  C and dew is absent, synoptic scale rainfall can be detected at 37 GHz. Spencer et al. (1983) reported that extremely low 37 GHz  $T_B$ s over land are indicative of heavy rainfall associated with thunderstorms, in which high concentrations of ice in the upper reaches of the thunderstorms act as volume scatters to upwelling radiation.

Using the polarization and frequency diversity of the Nimbus 7 Scanning Multichannel Microwave Radiometer (SMMR) and implementing statistical techniques, several investigators developed rainfall retrieval algorithms for land surfaces which were able to screen out wet land from rainfall (Rodgers and Siddalingaiah, 1983; Spencer, 1984). Spencer and Santek (1985) improved this type of multichannel/polarization algorithm by isolating and removing the effects of variations in thermometric surface temperature, soil moisture, and snow cover on the measured microwave  $T_B$ s.

On June 19, 1987, the Department of Defense launched a Defense Meteorological Satellite Program (DMSP) polar orbiting satellite which carried the first Special Sensor

Microwave/Imager (SSM/I). This instrument measures four frequencies (19.35, 22.235, 37, and 85.5 GHz), with dual polarization for three of the four (only vertical polarization is measured at 22 GHz). The 85 GHz channels represent the highest frequency and highest resolution microwave field-of-view ever flown on a satellite (see Table 1.1). The 85 GHz channels were expected to improve global precipitation monitoring capabilities, especially over land. Preliminary attempts at utilizing SSM/I measurements have provided encouraging results. The SSM/I 85 GHz channel is sensitive to volume scattering by precipitation and ice within a cloud which results in low  $T_B$ s. By making use of the polarization diversity at 85 GHz to discriminate precipitation from the surface background, a polarization corrected temperature (PCT) can be formulated which isolates the precipitation (Spencer, et al, 1989). A PCT represents a hypothetical  $T_B$  that a surface would emit solely due to the presence of an atmosphere. Therefore, the PCT of a precipitating cloud is lower than that of a cloudy non-precipitating region because of the strong volume scattering affects of precipitation. Spencer empirically found that 85 GHz PCTs less than 255 K generally denote precipitation areas. PCTs are useful for both ocean and land background situations and in areas with land-water boundaries since PCTs are a measure of volume scattering rather than of surface emissivity.

A problem with a sequence of frequencies on a microwave sensor is that their instantaneous fields of view (IFOV) are not the same, as illustrated in Figure 1.1. To ensure that the signal to noise ratio is large enough to compensate for the low energy levels emitted by the earth and atmosphere, lower frequencies must have larger IFOVs. Recently, this problem has been overcome by deconvolution procedures which can be used to match the spatial resolution of the various frequencies (Olson, 1986; Farrar and Smith, 1992; Robinson et al., 1991). Deconvolution procedures introduce noise into the data, but steps can be taken to insure that these effects are minimized (Farrar, 1991). By

TABLE 1.1: SSM/I Channel footprint dimensions.

Frequency (GHz)	Polarization	Footprint (km)	
		A.T.	C.T.
19.35	Vertical	69	43
19.35	Horizontal	69	43
22.235	Vertical	50	40
37.0	Vertical	37	28
37.0	Horizontal	37	29
85.5	Vertical	15	13
85.5	Horizontal	15	13

A.T. is Along Track, C.T. is Cross Track

using deconvolution procedures, spatial resolutions at different frequencies can be matched, facilitating direct comparisons between measurements at distinct frequencies.

Polar orbiting, sun-synchronous satellites such as the DMSP only pass over a given location twice a day, so sampling problems arise due to the diurnal variability of precipitation. Sampling errors over oceanic regions, based on two satellite samples per day to obtain monthly rainfall, can be shown to have an error of about 10% (Bell, et al. 1990). In contrast, Seed and Austin (1990) showed that satellite sampling of precipitation over Florida, if sampled only twice per day, would result in errors as large as 130% for daily precipitation. If the same sampling is used to obtain a monthly areal average, the error drops to 22%. For a weekly areal average, such as used in this study, satellite sampling errors of rainfall in excess of 22% can be expected.

Another problem associated with satellite monitoring of precipitation at microwave frequencies, is the beam filling error. This occurs when an FOV does not contain homogeneous cloud optical properties. That is, it may be composed of varying amounts of clear sky, cloud, and rain, thus leading to a measurement representing the combined effect of the cloud, rain and surface background. Beam filling errors result in rain rates that are necessarily underestimated in emission algorithms due to the underlying non-linear relationship between brightness temperature and rainrate (Smith and Kidder, 1978).

Up to now, all techniques which have been reviewed represent instantaneous rainrate schemes. To understand how much rain falls in a week, a month, or some extended time period over a given area, other techniques can be used. Shin et al. (1990) developed an area-time averaged rainrate retrieval scheme to get monthly averages of precipitation over  $5^{\circ} \times 5^{\circ}$  oceanic regions, using ESMR-5 19 GHz data obtained during GATE, in which the raw  $T_{\text{ps}}$  were first collected into histograms. The shapes of the

histograms suggested that they were composed of a normal distribution of temperatures from the ocean background (the width of the distribution being partly related to channel noise) and a skewed distribution of precipitation at higher  $T_B$ s. By application of a statistical estimation scheme to identify the background distribution, which can then be separated from the overall histogram, the rain distribution can be isolated. Brightness temperatures of the rain-only distribution are converted to rainrates based upon an exponential form of the brightness temperature - rainrate relationship, developed by Wilheit (1977), a estimate of the freezing level, and the background temperature represented by the peak of the histogram.

Durkee (1980) developed a histogram technique to estimate summer precipitation frequency over the north central United States using ESMR-6 37 GHz data. The shape of the  $T_B$  histogram was represented by a normal distribution of non-raining pixels and a skewed distribution towards colder  $T_B$ s of raining pixels. The deviations from the mean of the normal portion of the distribution reflect variations of the contribution from the atmosphere and surface conditions. Any pixels greater than two standard deviations from the mean of the normal portion of the histogram are identified as rain. Although this study did not calculate rainrates, it did relate the  $T_B$  histograms to precipitation frequency and correlated the results with observed raingage data, which produced satisfactory results except in the northeast portion of the north central United States.

A multichannel, area-time histogram oceanic precipitation retrieval scheme using the 19 and 22 GHz frequencies of the SSM/I has recently been developed by Wilheit et al. (1991) to estimate monthly rainfall. The method uses the two frequencies in a linear combination to offset the effects of water vapor variability and to estimate rain layer thickness based on simplified theoretical calculations of an idealized rain layer from the

Wilheit et al. (1977) study. The technique is based upon a lognormal representation of the probability distribution function of rainfall intensity, which is used in a forward RTE model to generate a predicted  $T_B$  histogram. The predicted histogram is compared to the observed  $T_B$  histogram for a given oceanic region, and the lognormal parameters (logarithmic mean rainrate, probability of non-zero rainrate, standard deviation of logarithmic rainrate) adjusted until the predicted  $T_B$  histogram matches the observed  $T_B$  histogram.

## 1.2 Motivation

Recent studies indicate that physically-based precipitation retrieval schemes can detect instantaneous rainrates and area-time averaged rainfall. However, the major successes are for oceanic retrievals stemming from the high contrast between precipitating clouds and the ocean background and the fact that rain layers produce the rain signal. Land-based retrievals have only had limited success because of the general lack of contrast between the land background and precipitation except when large ice particles are present. In that case rain estimates are only indirect. The main scientific objective of this study is to methodically and quantitatively determine how much contrast does exist between raining and non-raining conditions for each of a large set of passive microwave parameters. Once the robustness of each of the parameters is quantified in terms of its relationship to rainfall, a statistical rainfall estimation algorithm is generated on a training data set from one partial year of data then validated on independent data sets from two different years. The seven channel/four frequency SSM/I microwave measurements along with Indian Geosynchronous Satellite (INSAT) infrared measurements serve as a starting point for this study. In



addition to the basic channel brightness temperatures, 12 additional parameters are created based upon the individual microwave channels. These include three unpolarized  $T_B$  quantities, three frequency dependent PCTs, three differential  $T_B$ s at vertical polarization, and three frequency dependent normalized degree of polarization quantities. Furthermore, the shapes of the histograms for the separate frequencies will be investigated. All of these parameters are listed in Table 1.2 and will be discussed, in depth, in section 4. The robustness of these parameters are tested against weekly precipitation totals from the subdivisional states of India during the summer monsoons of 1987, 1988, and 1989.

The precipitation regime of the Indian summer monsoon was chosen because of its diverse rainfall characteristics. Indian monsoon precipitation is highly organized on a variety of time and space scales. In addition, the magnitude of rainfall accumulation over a week, is highly variable between weeks and regions due to factors such as topography, latitude, continentality, and the phase of the monsoon. The character of precipitation across India also shows variability with showery precipitation in the north to more constant rains in the south (Ramage, 1971). Strong intra-seasonal variability at various time scales related to northward propagating low frequency modes, quasi-periodic formation of monsoon depressions, and the quasi-periodic passage of synoptic-scale waves are well known features of the monsoon. The most well known intra-seasonal variation, is the monsoon burst-break sequence, which is likely induced by the resonance of two distinct intra-seasonal modes. Significant inter-annual variability in monsoon rainfall also occurs and is triggered by variation in the large scale circulation. For example, the Indian monsoon season of 1987 is considered to be a year of deficient rainfall (Das, et al., 1988), whereas the monsoon seasons of 1988 and 1989 provided the highest and second highest rainfalls of the decade (Das. et al., 1989; Gupta, et al., 1990).

TABLE 1.2: Definition of microwave and IR parameters.

19V

19H

22V

37V

37H

85V

85 H

$$19U = (19V + 19H)/2$$

$$37U = (37V + 37H)/2$$

$$85U = (85V + 85H)/2$$

$$19 \text{ PCT} = 2.4(19V) - 1.4(19H)$$

$$37 \text{ PCT} = 2.1(37V) - 1.1(37H)$$

$$85 \text{ PCT} = 1.82(85V) - 0.82(85H)$$

$$19/22\text{DIF} = 19V - 22V$$

$$19/37\text{DIF} = 19V - 37V$$

$$19/85\text{DIF} = 19V - 85V$$

$$19\text{NDP} = (19V - 19H)/19U$$

$$37\text{NDP} = (37V - 37H)/37U$$

$$85\text{NDP} = (85V - 85H)/85U$$

INSAT IR

## CHAPTER 2

### Methodology

#### 2.1 Probability Distribution Function Formation

The 35 subdivisional states of India shown in Figure 2.1 extend over the region being used to examine the robustness of microwave and infrared parameters for detection of time-area averaged rainfall over land. In order to assemble the satellite measurements into the proper subdivisional states, the boundaries of each subdivision are first determined by latitude and longitude coordinates which are entered into a non-uniform grid file. Since microwave  $T_B$ s exhibit significantly different signatures depending upon whether the pixel is located over land or water, steps must be taken to ensure that pixels contaminated by water along coastlines are eliminated. Therefore,  $T_B$  data within 60 km of a coastline have been removed from the grid file. The Andaman and Nicobar Island Chain (subdivision 1), and the Lanshadweep Island Group (subdivision 35) were removed because pixels over these subdivisions at microwave frequencies do not contain a significant number of land pixels devoid of oceanic contamination.

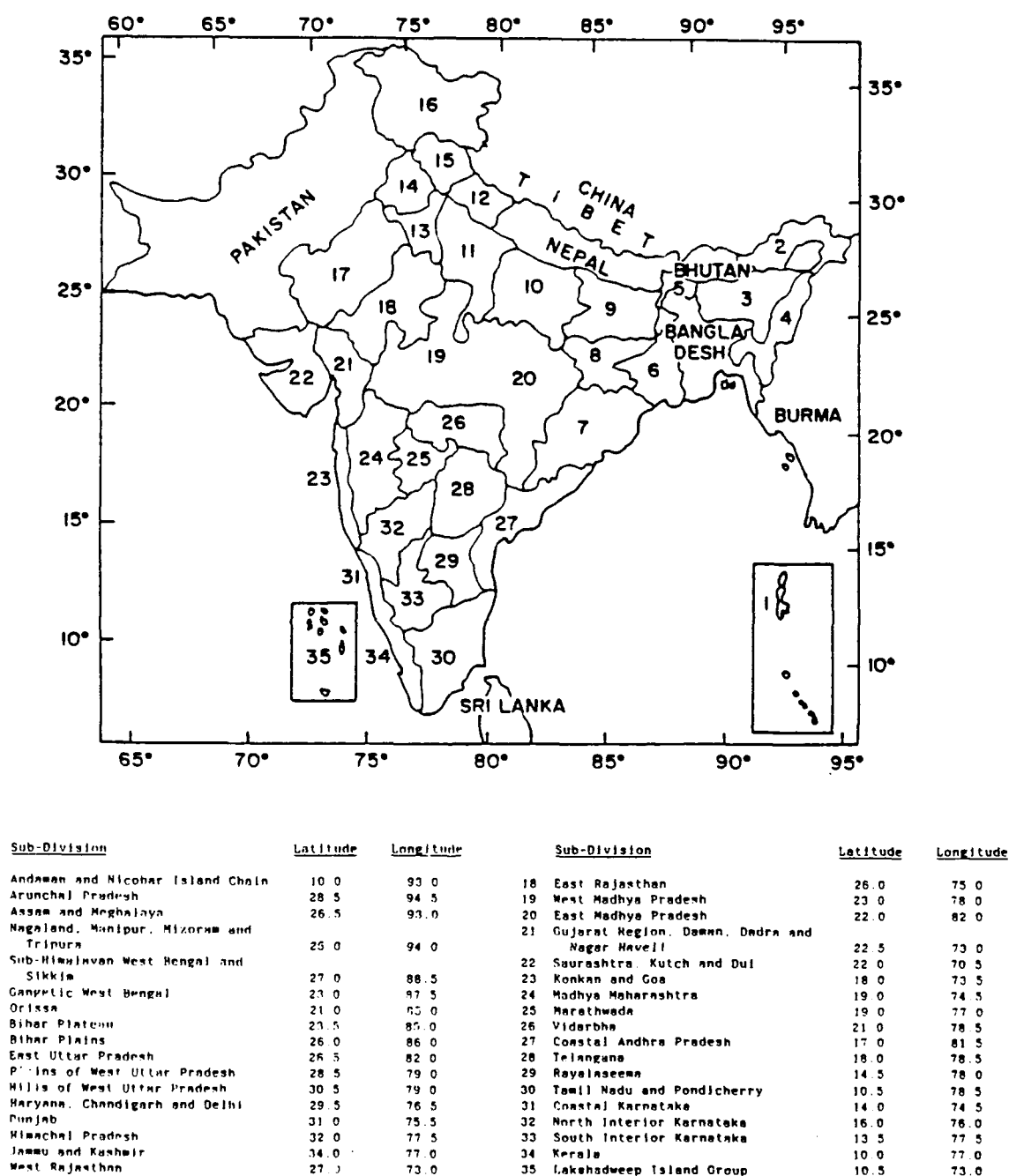


Figure 2.1: Indian subdivisions used for weekly rainfall totals.

Before the SSM/I measurements are mapped to the subdivisions, the measurements are deconvolved to the spatial resolution of the 85 GHz channel. Once the measurements are deconvolved and the subdivision grid file defined, the data are mapped to the subdivisional states in a non-ambiguous way. Given the mapping, histograms of brightness temperature are created by counting the number of times each brightness temperature occurs in a given subdivision over a period of one week. The histograms are then normalized by dividing the individual frequencies by the total frequency within a complete histogram. This defines a probability distribution function (PDF) of  $T_B$ s with the normalization allowing for straightforward PDF comparisons between different sized subdivisions and different sample counts in the histograms.

Probability distribution functions have been produced by subdivision for each of the seven SSM/I frequencies, and twelve frequency combinations on a 1-week basis, treating morning and evening data separately for the Indian monsoon seasons of 1987 through 1989. In terms of nomenclature, the seven SSM/I frequencies and twelve frequency combinations will be referred to as parameters, in which M and E subscripts are attached to the parameters to designate morning and evening time periods, respectively. In India, morning orbits range in time between 2200-0200 GMT (0330-0730 MST) and evening orbits range from 1100-1500 GMT (1630-2030 MST).

In addition to the SSM/I parameters, INSAT IR measurements have been mapped to the subdivisional grid and subsequently formed into PDFs in the same manner as the SSM/I parameters. The main differences between the SSM/I and INSAT data sets are that the IR measurements are available twice daily in 1987, eight times daily in 1988, but not at all during 1989.

## 2.2 Quality Control Procedures

Although steps were taken to remove ocean contamination from pixels along coastlines, PDFs were also visually checked to ensure contamination did not occur due to satellite navigation errors. Specifically, 19 GHz PDFs that contained secondary peaks at low  $T_B$ s which did not fluctuate with time were deleted from the data set. These secondary peaks are representative of pixels which contain ocean areas which appear radiometrically cold when compared to land surfaces. Figure 2.2 and 2.3 help illustrate the ocean contamination problem. Figure 2.2 shows 20 weeks of  $19V_E$  PDFs for the Konkan and Goa region (subdivision 23). Secondary peaks at about 220 K are evident throughout the 20 weeks and are most pronounced during the first 5 weeks (days 119-153) when little to no rain fell in the region. In comparison, Figure 2.3 contains 20 weeks of  $19V_E$  PDFs for Madhya Maharashtra (subdivision 24) which is located inland and adjacent to the Konkan and Goa region. None of these PDFs exhibit secondary peaks associated with low emissivity ocean surfaces. This data elimination procedure resulted in removing Gangetic West Bengal (subdivision 6), Saurashtra, Kutch, and Dui (subdivision 22), Konkan and Goa (subdivision 23), Coastal Karnataka (subdivision 31), and Kerala (subdivision 34), from the data set.

Mountain regions, sometimes covered by snow, also presented problems because their PDFs are strikingly different from PDFs in the remaining subdivisions of India. Snow varies in emissivity depending upon whether it is characterized as dry or moist. Dry snow has low emissivity which approaches the emissivity of a water surface, whereas moist snow has emissivities nearly equal to that of dry land (Wilheit, 1972). These PDFs are characterized by a broad range of  $T_B$ , caused by combinations of dry and moist snow mixed in with precipitation and other types of land surfaces, with a

19 GHZ VERTICALLY POLARIZED  
AREA 23 EVENING DATA

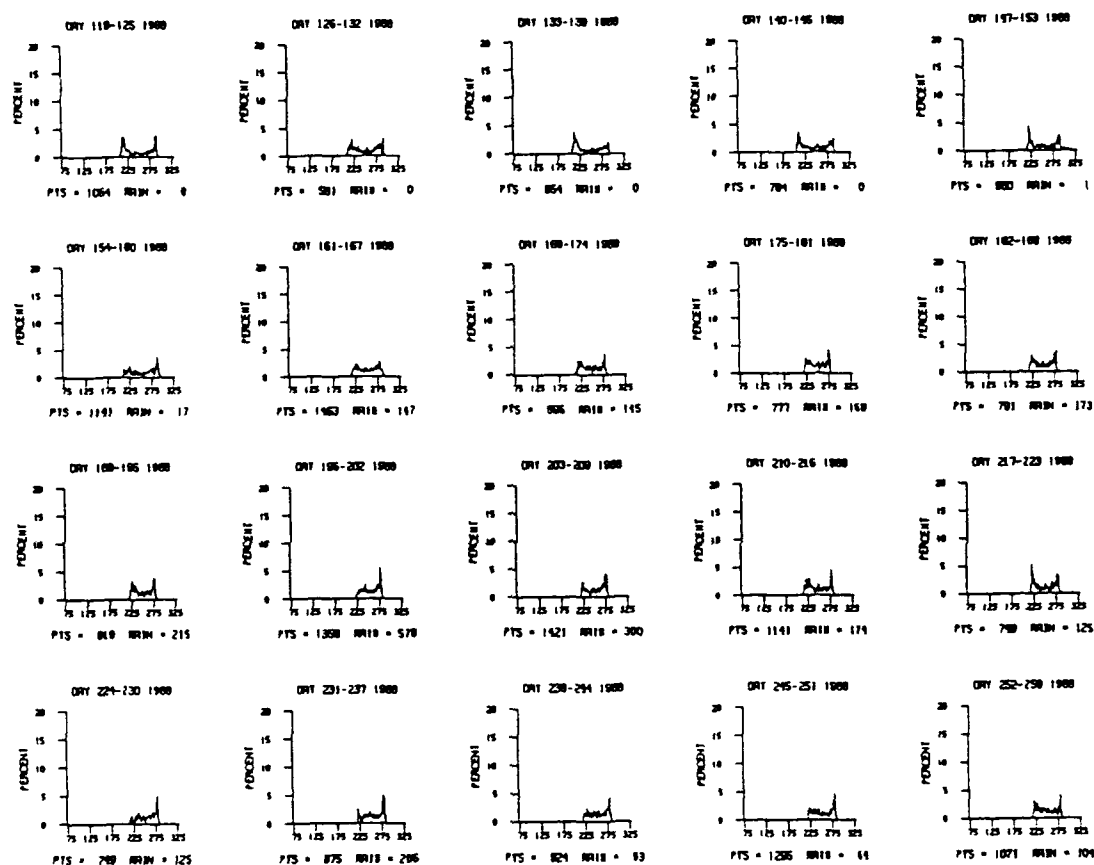


Figure 2.2: 19VE probability distribution functions for 20 weeks in 1988 for Konkan and Goa. Low  $T_B$  peak represents pixels containing ocean contamination.

19 GHZ VERTICALLY POLARIZED  
AREA 24 MORNING DATA

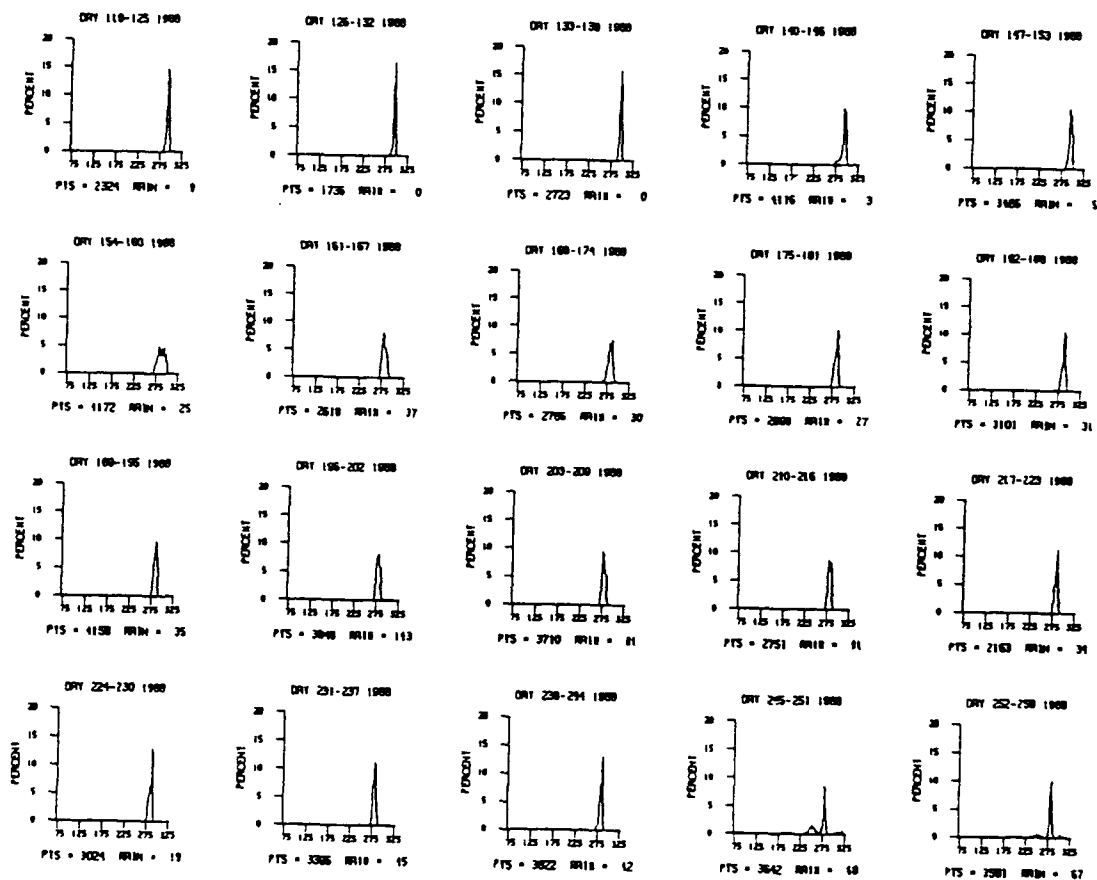


Figure 2.3: 19VE probability distribution functions for 20 weeks in 1988 for Madhya Maharashtra illustrating typical non-contaminated 19 GHz probability distribution functions.



minor peak related to the land background at high  $T_B$ . Figure 2.4 contains 20 weeks of  $37V_E$  PDFs for Jammu and Kashmir (subdivision 16) which has a bimodal distribution which can be used to identify regions containing snow. The distribution of cold  $T_B$  has a mean near 225 K and is composed of FOVs containing dry snow. As summer approaches the cold  $T_B$  distribution shrinks and the mean of the entire PDF warms. However, a significant number of pixels exhibit cold  $T_B$ s representative of FOVs containing either moist snow on the surface or rain. In contrast, Figure 2.5 contains the  $37V_E$  PDFs for East Rajasthan (subdivision 18) which is located in north central India and shows the monomodal shape characteristic of 37 GHz PDFs. The peak of the monomodal distribution in East Rajasthan is located near 275 K and can also be seen in Jammu and Kashmir as a minor peak, which is representative of a snow-free land surface. The subdivisions removed by this process include Arunchal Pradesh (subdivision 2), Hills of West Uttar Pradesh (subdivision 12), Himachal Pradesh (subdivision 15), and Jammu and Kashmir (subdivision 16). In total, 11 subdivisions have been deleted from the data set, because of either ocean or snow contamination.

In addition to water-snow contamination quality checks, data quality checks were made to eliminate weeks with significant bad data or insufficient satellite coverage during 1988. Significant amounts of bad data can be detected by analyzing the mean of the vertical polarization difference between 19V and 22V (19/22DIF). This parameter is useful in detecting bad data because it has a narrow range of variation associated with it and so large deviations are readily discernable. This parameter revealed 3 weeks in which the weekly subdivisional means were greater than 3 standard deviations from the grand mean in every subdivision. Because this occurred in every subdivision for the same 3 weeks regardless of rainfall, it is assumed that bit dropouts or pixel mislocation errors had impacted those data.

37 GHZ VERTICALLY POLARIZED  
AREA 16 EVENING DATA

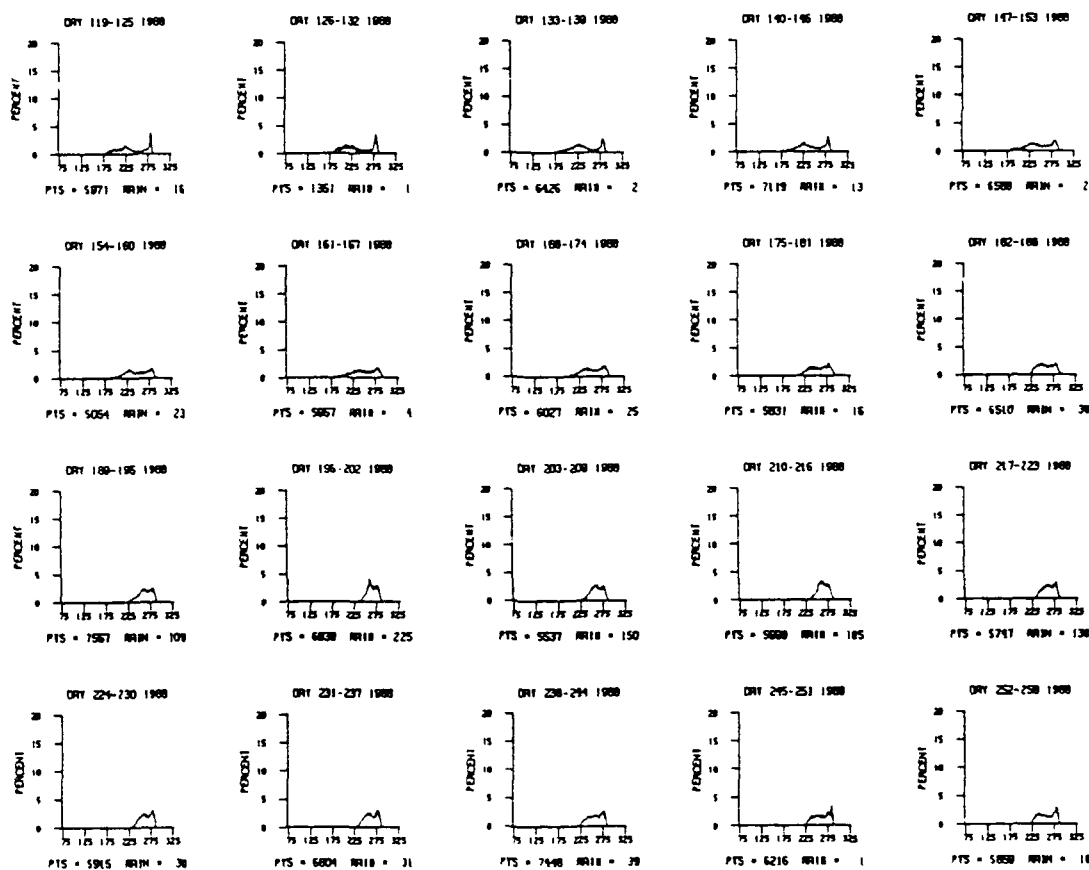


Figure 2.4: 37VE probability distribution functions for 20 weeks in 1988 for Jammu and Kashmir illustrating affects of snow on 37 GHz probability distribution functions.

37 GHZ VERTICALLY POLARIZED  
AREA 18 EVENING DATA

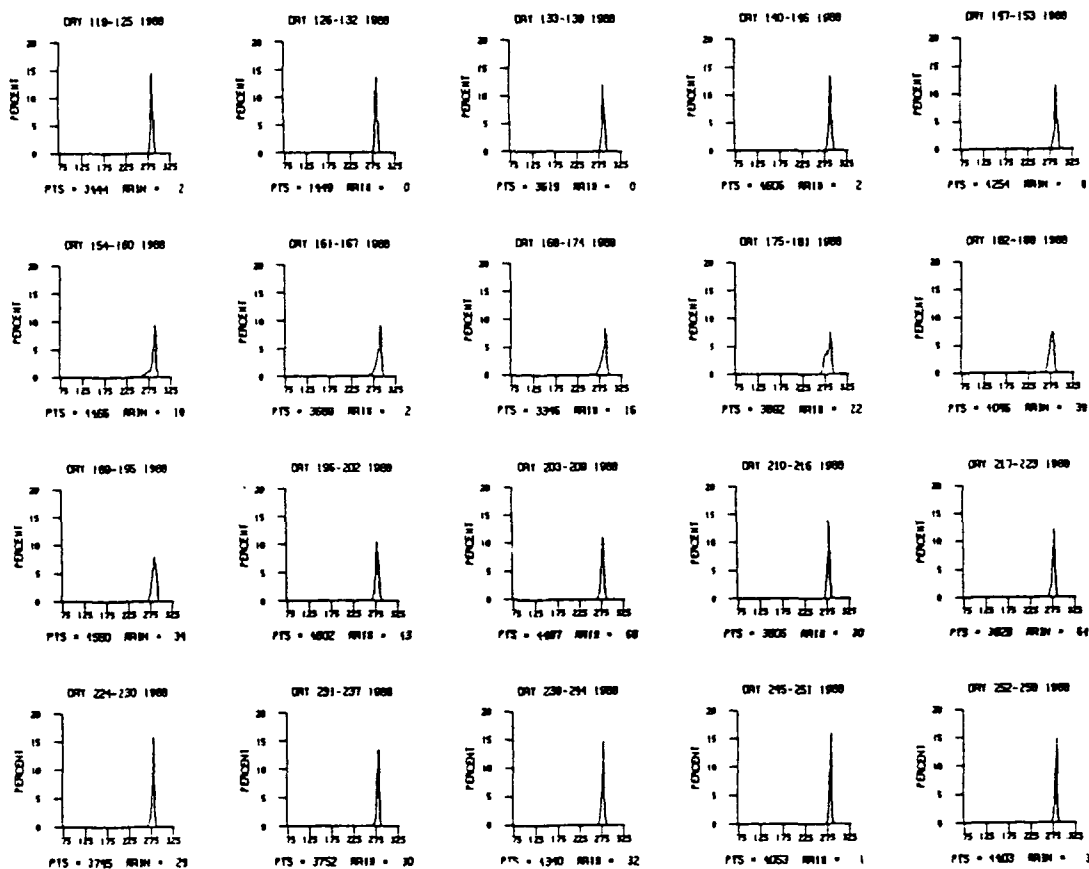


Figure 2.5: 37VE probability distribution functions for 20 weeks in 1988 for East Rajasthan illustrating typical 37 GHz probability distribution functions.

Finally, a check for insufficient satellite coverage was applied. If the largest number of pixels in a given subdivision and week for the entire six month season represents full satellite coverage, then any week which had less than 15% of full coverage was eliminated. The above two final checks result in 4 weeks of eliminated data for 1988.

### 2.3 Robustness of Individual Parameters

To determine the robustness of individual parameters, four variables based upon each parameter are considered. The first two are defined from the means and standard deviations of each microwave and infrared parameter PDF. The other two are defined from cumulative distribution functions (CDF) created by associating the number of pixels at each  $T_B$  coordinate within a PDF with the cumulative count from the cold end. From the CDF, slope and intercept factors are obtained. The slope factor is determined by measuring the gradient of  $T_B$  accumulation over the range of  $T_B$ s within the CDF. The intercept factor is defined as the coldest  $T_B$  present within a CDF.

In regards to nomenclature, the mean and standard deviation of a PDF and the slope and intercept factors of a CDF will be referred to as variables. The four variables are used to test the robustness of each microwave and infrared parameter against measured subdivisional weekly rainfall.

For a one parameter least squares linear regression test of robustness, the coefficient of determination ( $R^2$ ) is used to calculate the correlation coefficient ( $R$ ). This quantity is then used as the criterion for evaluating microwave and infrared

parameter performance of a given variable (mean, slope factor, etc.).  $R^2$  is calculated as:

$$R^2 = 100(1 - \frac{SSE}{SST}) \quad (1)$$

where SSE is the error sum of squares, SST is the total sum of squares and the correlation coefficient is found by taking the square root. All statistics calculations used in this paper were obtained from the IMSL statistics library (IMSL, 1989).

#### 2.4 Robustness of Multi-parameter Combinations

The coefficient of determination ( $R^2$ ) increases as new parameters are added to a regression model, however a larger  $R^2$  is not necessarily indicative of a better model. If the error sum-of-squares in the new combination does not decrease by an amount equal to the original combination mean square error (the sum of a multi-parameter squared bias plus its variance), the new combination will have a larger mean square error due to the loss of one degree of freedom for error, thus resulting in a worse regression. For this reason, an adjusted coefficient of determination called  $R_a^2$  (defined below), is used to calculate the correlation coefficient since it does not necessarily increase as additional parameters are introduced. The definition of  $R_a^2$  is given by (Montgomery and Peck, 1982):

$$R_a^2 = 100[1 - (\frac{n-1}{n-p-1}) (\frac{SSE}{SST})] \quad (2)$$

where  $n$  is the number of observations, and  $p$  the number of regressors.

## 2.5 Testing of Single and Multi-parameter Models on Independent Data Sets

The results obtained during the 1988 monsoon season are validated on independent data sets from the 1987 and 1989 monsoon seasons. To determine how individual parameters compared to the 1988 training data set, an unadjusted  $R^2$  is calculated from the independent data sets, which in turn yields (R) the correlation coefficient. Multi-parameter model validation is accomplished by applying the optimal regression model from the 1988 satellite measurements to the 1987 and 1989 measurements, and then analyzing the differences in correlation coefficients against those obtained from independent regression models from 1987 and 1989. For 1989, the optimal regression model, referred to as WO85V, is calculated without parameters containing the 85V channel because this channel completely degraded after late 1988. As a result, 85V, 85U, 85PCT, 19/85DIF, and 85NDP must be eliminated from the 1989 analysis. Thus, two regression models have been obtained from the 1988 data training set, one for use with 1987 (the optimal model) and the other for 1989 (the WO85V model).

## **CHAPTER 3**

### **Data Sources**

The data used in this study include Indian subdivisional weekly rainfall, passive microwave measurements from the DMSP SSM/I instrument, and INSAT infrared measurements.

#### **3.1 Indian Subdivisional Rainfall**

Indian subdivisional weekly rainfall data were obtained from the Indian Meteorological Department's Weekly Rainfall Reports. [These were kindly provided by the staff librarian at the National Center for Atmospheric Research.] The data consist of weekly averages of rainfall recorded at raingages for each of India's 35 subdivisions (Figure 2.1) for the inclusive periods: Jul 9 - Oct 28, 1987 (16 weeks); Apr 28 - Oct 26, 1988 (26 weeks); and May 4 - 25, Oct 1989 (25 weeks). The dates for each week are listed in Tables 3.1 for 1987, 1988, and 1989.

Table 3.1: Weeks used in 1987, 1988, and 1989 for this study.

## 1987

9 - 15 Jul	3 - 9 Sep
16 - 22 Jul	10 - 16 Sep
23 - 29 Jul	17 - 23 Sep
30 Jul - 5 Aug	24 - 30 Sep
6 - 12 Aug	1 - 7 Oct
13 - 19 Aug	8 - 14 Oct
20 - 26 Aug	15 - 21 Oct
27 Aug - 2 Sep	22 - 28 Oct

## 1988

28 - 4 May	28 Jul - 3 Aug
5 - 11 May	4 - 10 Aug
12 - 18 May	11 - 17 Aug
19 - 25 May	18 - 24 Aug
26 May - 1 Jun	25 - 31 Aug
2 - 8 Jun	1 - 7 Aug
9 - 15 Jun	8 - 14 Sep
16 - 22 Jun	15 - 21 Sep
23 - 29 Jun	22 - 28 Sep
30 Jun - 6 Jul	29 Sep - 5 Oct
7 - 13 Jul	6 - 12 Oct
14 - 20 Jul	13 - 19 Oct
21 - 27 Jul	20 - 26 Oct

## 1989

4 - 10 May	3 - 9 Aug
11 - 17 May	10 - 16 Aug
18 - 24 May	17 - 23 Aug
25 - 31 May	24 - 30 Aug
1 - 7 Jun	31 Aug - 6 Sep
8 - 14 Jun	7 - 13 Sep
15 - 21 Jun	14 - 20 Sep
22 - 28 Jun	21 - 27 Sep
29 Jun - 5 Jul	28 Sep - 4 Oct
6 - 12 Jul	5 - 11 Oct
13 - 19 Jul	12 - 18 Oct
20 - 26 Jul	19 - 25 Oct
27 Jul - 2 Aug	



### 3.2 Passive Microwave SSM/I Measurements

The SSM/I measurements used in this project were obtained from antenna temperature data tapes produced by Remote Sensing Systems (Wentz, 1991) and provided by NASA. The basic SSM/I data set produced for this project consists of brightness temperatures for each of the seven channels over the Indian subcontinent and surrounding waters. The brightness temperatures are all deconvolved to the spatial resolution of 85 GHz channels (15 km x 13 km). Each PDF contains one week of data for each of the parameters listed in Table 1.2 coinciding with the weekly rainfall reports of the Indian Meteorology Agency.

### 3.3 INSAT Infrared Measurements

The INSAT infrared (IR) measurements used in this project were obtained from the Indian Meteorological Department (IMD) through the U. S. National Science Foundation under the auspices of the Indo-US Science and Technology Exchange Program (Smith et al., 1988). The data set consists of reduced resolution (22 km) IR measurements corresponding to the dates of the available Indian subdivisional rainfall reports as described in section 3.1 and bounded by the region described in section 3.2. Normally IR measurements are available two times per day at 0600 and 1200 GMT for 1987 and eight times per day at 0000, 0300, 0600, 0900, 1200, 1500, 1800, and 2100 GMT for 1988. Lamm et al. (1991), has provided a detailed description of the INSAT data, including the calibration and navigation procedures.

## CHAPTER 4

### Analysis of Microwave and Infrared Variables

In this section, the properties of the microwave (MW) PDFs and CDFs and IR PDFs will be examined in detail. This involves the means and standard deviations of the MW PDFs, the means of the IR PDFs, and the slope and intercept factors of the MW CDFs. Then, multi-parameter regression models will be built to evaluate how individual MW and IR parameter variables behave in conjunction with other MW and IR parameter variables.

#### 4.1 Robustness Analysis of Individual Parameters

**4.1.1 Properties of the microwave probability distribution functions.** The mean of each parameter PDF is used to estimate the measured area-averaged rainfall in each subdivision during one week. The mean of a PDF of a particular parameter represents the average value of the samples in the distribution. The units of the average brightness temperatures, polarization corrected temperatures, or polarization difference temperatures are in degrees Kelvin. For the frequency dependent normalized degree of polarization parameters, the mean represents a non-dimensional quantity. Scatter diagrams of the means of the PDFs of a given parameter versus measured subdivisional

rainfall show that, in most cases (except 19NDP and 37NDP), rainfall increases as the mean of the parameter decreases. However, the means tend to decrease slower as the weekly rainfall amounts increase, particularly above 200 mm. The underlying behavior of the scatter diagrams becomes difficult to interpret beyond 200 mm because there are so few events at these higher totals, thus revealing the limited sampling capabilities of polar-orbiting satellites. Additionally, at very low rain rates, the mean exhibits a significant amount of scatter. Part of this is due to the wide variety of background radiances emanating from the surface due to surface temperature, hydrologic and orographic variability within and among subdivisions.

Figure 4.1 illustrates the variation of the parameter means in terms of the correlation coefficient for the morning and evening MW parameters. Table 4.1 lists the correlation coefficients and the root mean square (RMS) error of the PDF means for the morning and evening parameters. From the results, it is evident that the evening MW measurements exhibit a 20 percent stronger correlation with the observed rainfall than do morning MW measurements, except for 85V, 85U, and 85PCT. No morning MW parameter has a correlation greater than 0.60, however, evening MW parameters have a few over this threshold (19V, 19U, 37U, 19/22DIF). In addition, the RMS errors associated with all the parameters are large, ranging from 35.12 to 46.56 mm. The higher rainfall totals contribute significantly to the size of these errors. In many of these cases when using the associated regression equation to estimate total measured rainfall, underestimates exceed 150 mm.

An analysis of the parameter means provides insight into how each behaves with respect to measured subdivisional weekly rainfall. The 19 GHz channels have the highest correlation for evening data of any MW frequency at that time. Figure 4.2a-d shows the scatter diagrams for 19V<sub>M</sub>, 19H<sub>M</sub>, 19V<sub>E</sub>, and 19H<sub>E</sub>. Figure 4.2b shows that the

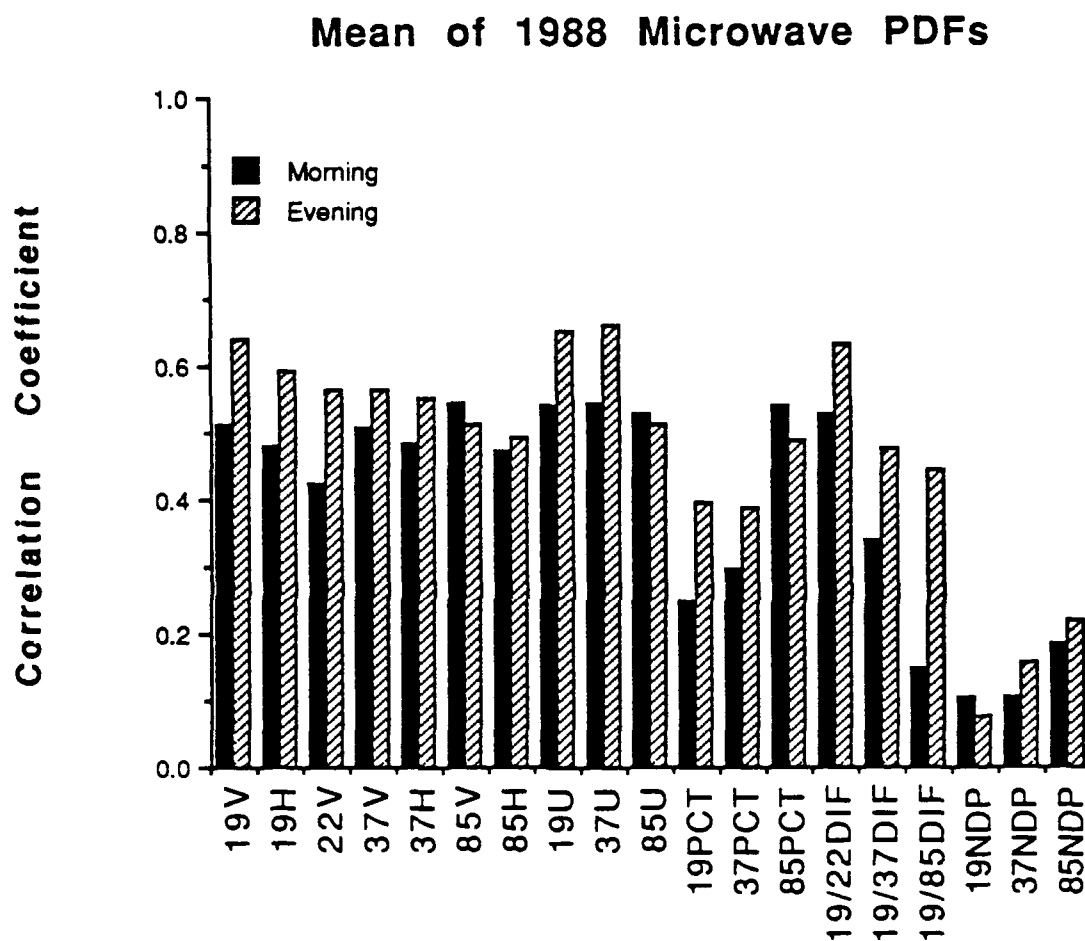


Figure 4.1: Correlation coefficient vs. microwave parameter. Mean of morning and evening microwave Probability Distribution Functions (1988).

Table 4.1: Correlation coefficients and RMS errors for the mean of the 1988 microwave PDFs.

<u>Parameter</u>	<u>Morning Orbits</u>		<u>Evening Orbits</u>	
	R	rms error	R	rms error
19V	-0.512	40.15	-0.638	35.96
19H	-0.482	40.96	-0.593	37.60
22V	-0.426	42.30	-0.562	38.64
37V	-0.510	40.21	-0.563	37.17
37H	-0.483	40.94	-0.554	38.89
85V	-0.546	39.17	-0.551	40.13
35H	-0.473	41.19	-0.493	40.64
19U	-0.538	39.40	-0.651	35.46
37U	-0.545	39.20	-0.659	35.12
85U	-0.527	39.72	-0.514	40.07
19PCT	-0.247	45.29	-0.397	42.87
37PCT	-0.294	44.67	-0.390	43.01
85PCT	-0.540	39.35	-0.488	40.77
19/22DIF	-0.527	39.72	-0.632	36.17
19/37DIF	-0.338	43.99	-0.477	41.03
19/85DIF	-0.149	46.23	-0.446	41.81
19NDP	+0.106	46.49	+0.076	46.56
37NDP	+0.103	46.50	+0.156	46.13
85NDP	-0.182	45.96	-0.219	45.56

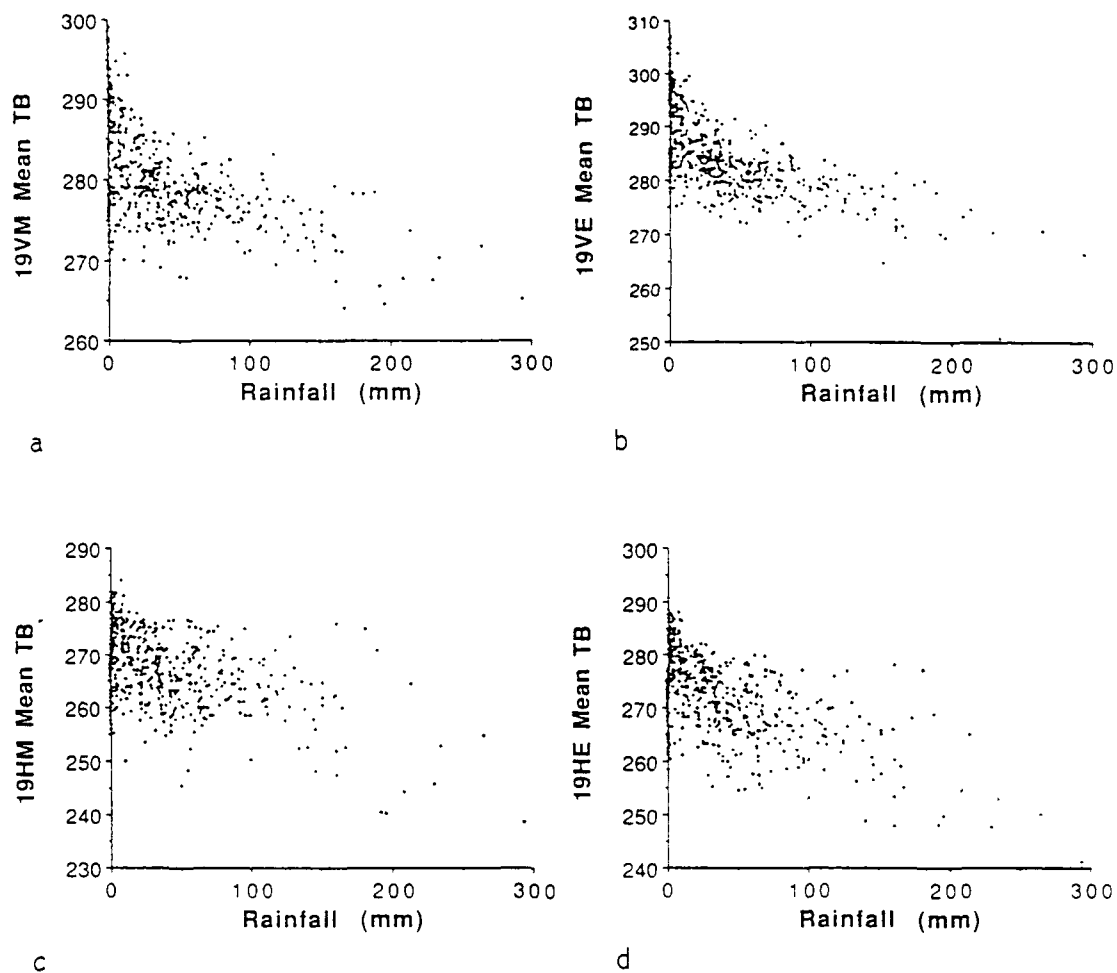


Figure 4.2: Scatter diagrams for a)  $19V_M$ , b)  $19V_E$ , c)  $19H_M$ , and d)  $19H_E$ .

scattering is most tightly grouped for  $19V_E$  in comparison to the other 19 GHz parameters. For all of the 19 GHz parameters, a clear decrease in the mean  $T_B$  occurs as rainfall increases. The sensitivity between low and high rainfall situations is in excess of 20 K for all 19 GHz parameters. These parameters are sensitive to variations in surface emissivity and relatively insensitive to surface temperature variations and since the measurements have been deconvolved, the affects of beam filling have been substantially reduced, thus leading to the relatively high correlation coefficients.

The lowest correlation of the first seven parameters (that is the individual channel mean  $T_B$ s) is found for  $22V_M$ . The mean of  $22V_E$  shows a stronger correlation but appears to be due to variations in  $T_B$  caused by surface heating near zero rainfall which shifts the intercept of the least squares fit to warmer  $T_B$ . The 22 GHz channel is sensitive to variations in atmospheric water vapor and therefore by itself, not a reliable parameter for detecting rainfall, because it responds similarly to precipitating and non-precipitating clouds. The scatter diagrams (Figure 4.3a-b), show that the mean of the 22V PDFs approach a lower limit near 280 K across the range of rainfall. This represents a loss of sensitivity due to the presence of water vapor when compared to the mean of 19 GHz channels.

Turning to 37 GHz channels scatter diagrams (Figure 4.4a-d), the decrease in the mean of the PDF in the vertical polarization  $T_B$ , with respect to rainfall, during the morning and evening reveals a sensitivity of about 10-15 K. The mean of the PDF of the horizontal channel has a slightly greater sensitivity of 15-25 K. The mean of the parameter  $37V_E$  ranks third among the first seven parameters, falling behind  $19V_E$  and  $19H_E$ . The mean of the parameters  $37H_M$  and  $37H_E$  exhibit significant scatter at mid-range rainfall totals (100-200 mm) as compared to the  $37V_M$  and  $37V_E$ . The amount of scatter at the mid-range rainfall totals may be indicative of the rainrate at the time of

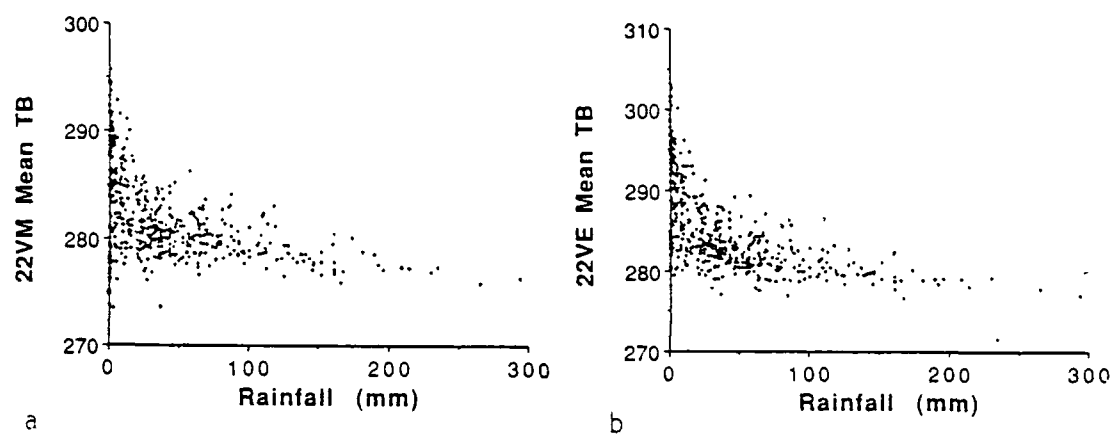


Figure 4.3: Scatter diagrams for a)  $22V_M$  and b)  $22V_E$ .



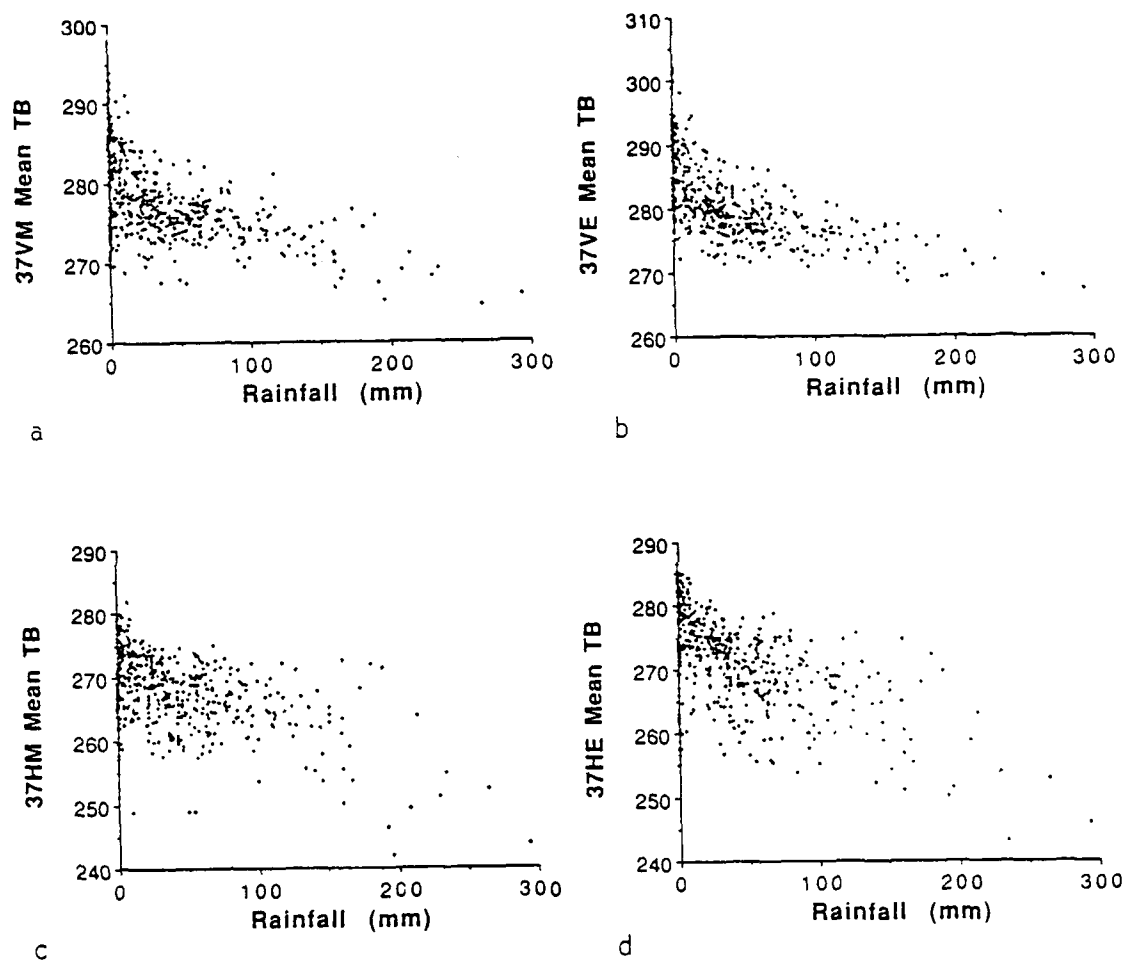


Figure 4.4: Scatter diagrams for a)  $37V_M$ , b)  $37V_E$ , c)  $37H_M$ , and d)  $37H_E$ .

measurement with higher  $T_B$  representing surface attenuation of the surface emission by light rainfall and lower  $T_B$  representing scattering caused by ice during heavy rainfall.

The 85 GHz channels are very sensitive to scattering caused by ice in the upper regions of precipitating clouds and are therefore a less direct measurement of rainfall for the case of cumulonimbus clouds. Oddly, the vertical and horizontal 85 GHz channels for evening data exhibit the lowest correlation coefficients of the first seven parameters (except for 22 GHz) but  $85V_M$  exhibits the highest correlation of the same parameters during the morning. Unlike these seven parameters, the difference between the morning and evening correlation coefficients is small. This suggests that the 85 GHz channel is less sensitive to diurnal fluctuations in rainfall. Figure 4.5a-d contain the scatter diagrams for the mean of the PDF for the 85 GHz parameters. The sensitivities of the 85 GHz parameters are less than those of the 37 GHz parameters, averaging about 10 K.

Before an evaluation of the remaining 12 parameters is made, an explanation of each is warranted. The first class of parameters (in terms of nomenclature, they are referred to as 19U, 37U, and 85U) are unpolarized brightness temperatures. They represent the average of the vertical and horizontal polarizations.

The mean of parameter  $19U_E$  has the second highest correlation coefficient (-0.651) of any morning or evening parameter mean. The scatter diagram (Figure 4.6b), shows a clear decrease in  $T_B$  with increasing area-averaged rainfall and a sensitivity of at least 20 K. This is due to the intrinsic properties of MW radiation at 19 GHz. At this frequency, for low rainrates, surface emission dominates the brightness temperature, but as rainfall increases attenuation of the surface emission increases leading to colder  $T_B$ s. The unpolarized parameters are desensitized to surface processes that induce

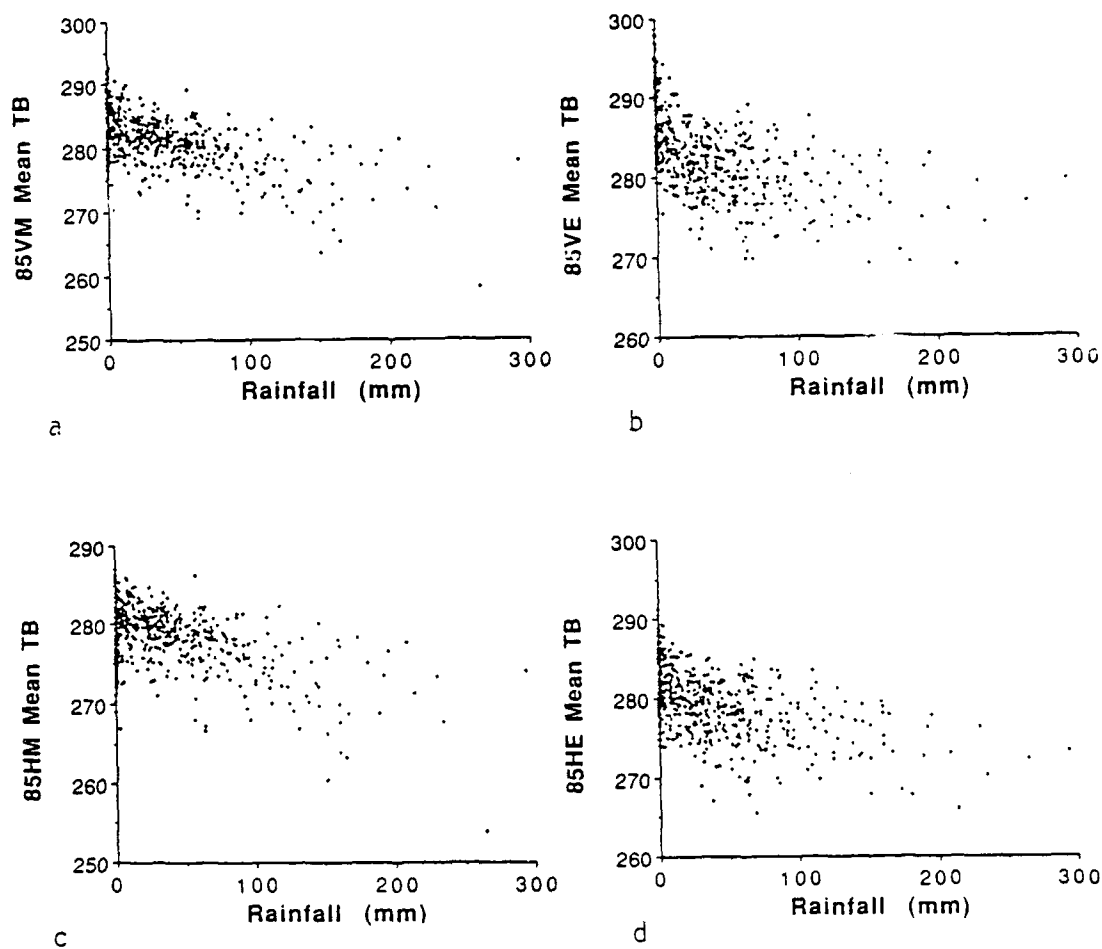


Figure 4.5: Scatter diagrams for a)  $85V_M$ , b)  $85V_E$ , c)  $85H_M$ , and d)  $85H_E$ .

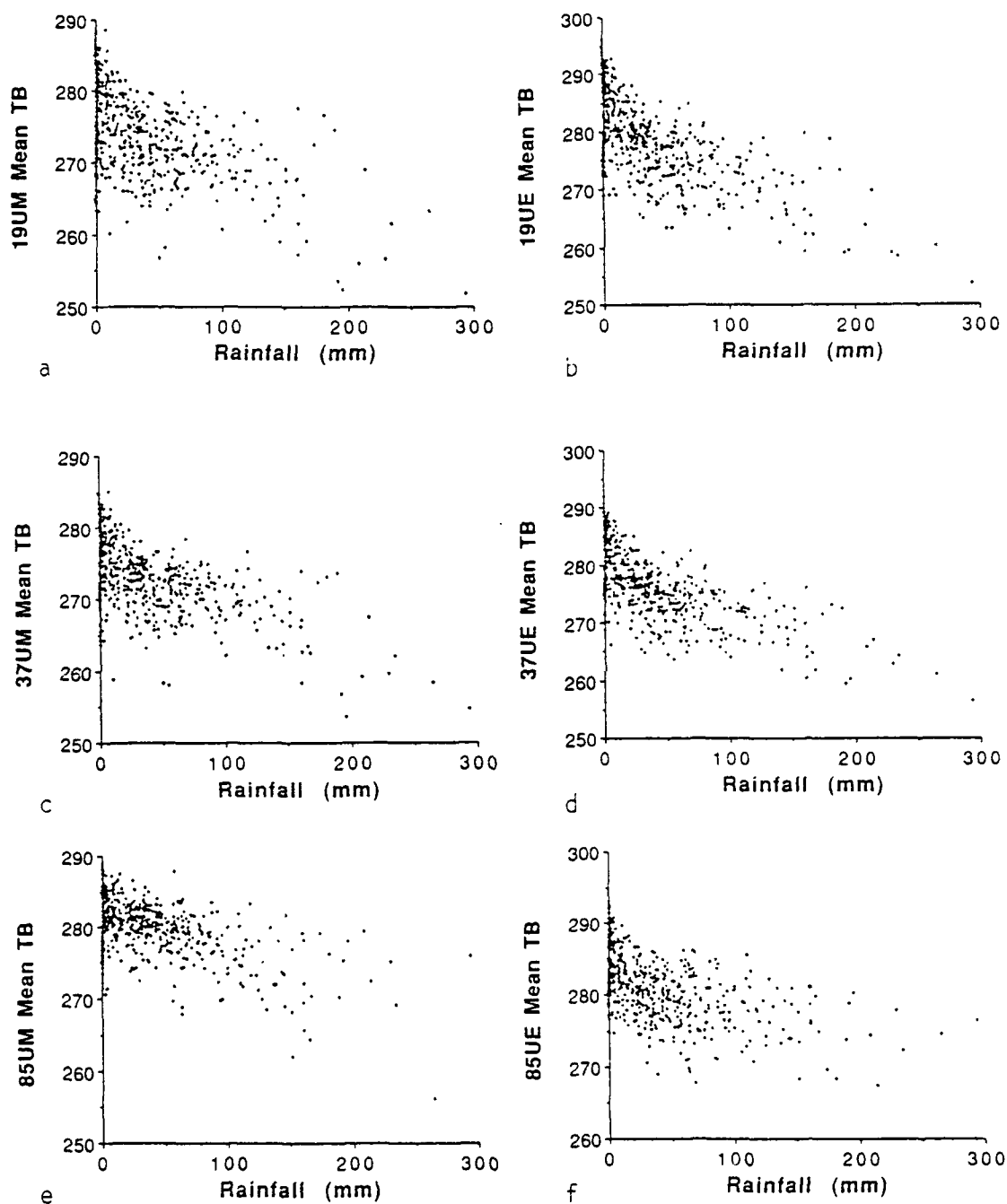


Figure 4.6: Scatter diagrams for a)  $19U_M$ , b)  $19U_E$ , c)  $37U_M$ , d)  $37U_E$ , e)  $85U_M$ , and f)  $85U_E$ .

polarization (soil moisture, vegetation cover, etc.). This can be seen by looking at the variance of the means of the PDFs of 19V, 19H, and 19U. Both 19V and 19H have higher  $T_B$  variance than does 19U. For evening data the variance is 67.3 and 74.4 for 19V<sub>E</sub> and 19H<sub>E</sub>, respectively versus 59.7 for 19U<sub>E</sub>.

The most robust parameter is 37U<sub>E</sub> with a correlation coefficient of -0.659. This intermediate frequency is affected by both emission and scattering depending upon the intensity of rainfall. At low rainrates surface emission is the dominant radiative feature. At higher rainrates, surface attenuation occurs and as the rainfall continues to increase, scattering becomes the dominant radiative feature due to large ice concentrations above the freezing level. Figure 4.6d shows that it has a sensitivity of more than 20 K.

The parameter 85U, although having a comparatively high correlation coefficient, does not provide any new information that can not already be attained by using the polarized 85 GHz channels separately (the correlation between 85U and 85V or 85H exceeds 0.965).

The next class of parameters is the PCT, which was described in section 1.1. PCTs are not robust parameters of area-time averaged rainfall over land. However, the correlation coefficients generally increase with increasing frequency because PCTs are primarily determined by volume scattering (in the presence of a scattering surface) which is readily detected at the higher frequencies. The scatter diagrams of each frequency dependent PCT parameter are shown in Figure 4.7a-f. From these diagrams, it can be seen that 19PCT and 37PCT occasionally exhibit very high mean  $T_B$ s at low rainfall totals. It may be possible that the coefficients for the vertical and horizontal channels in the PCT formulation may not be optimal for use over India.

Differential  $T_B$ s at vertical polarization between 19 GHz and 22, 37 and 85 GHz provides another class of parameter to test for robustness. For terminology in this

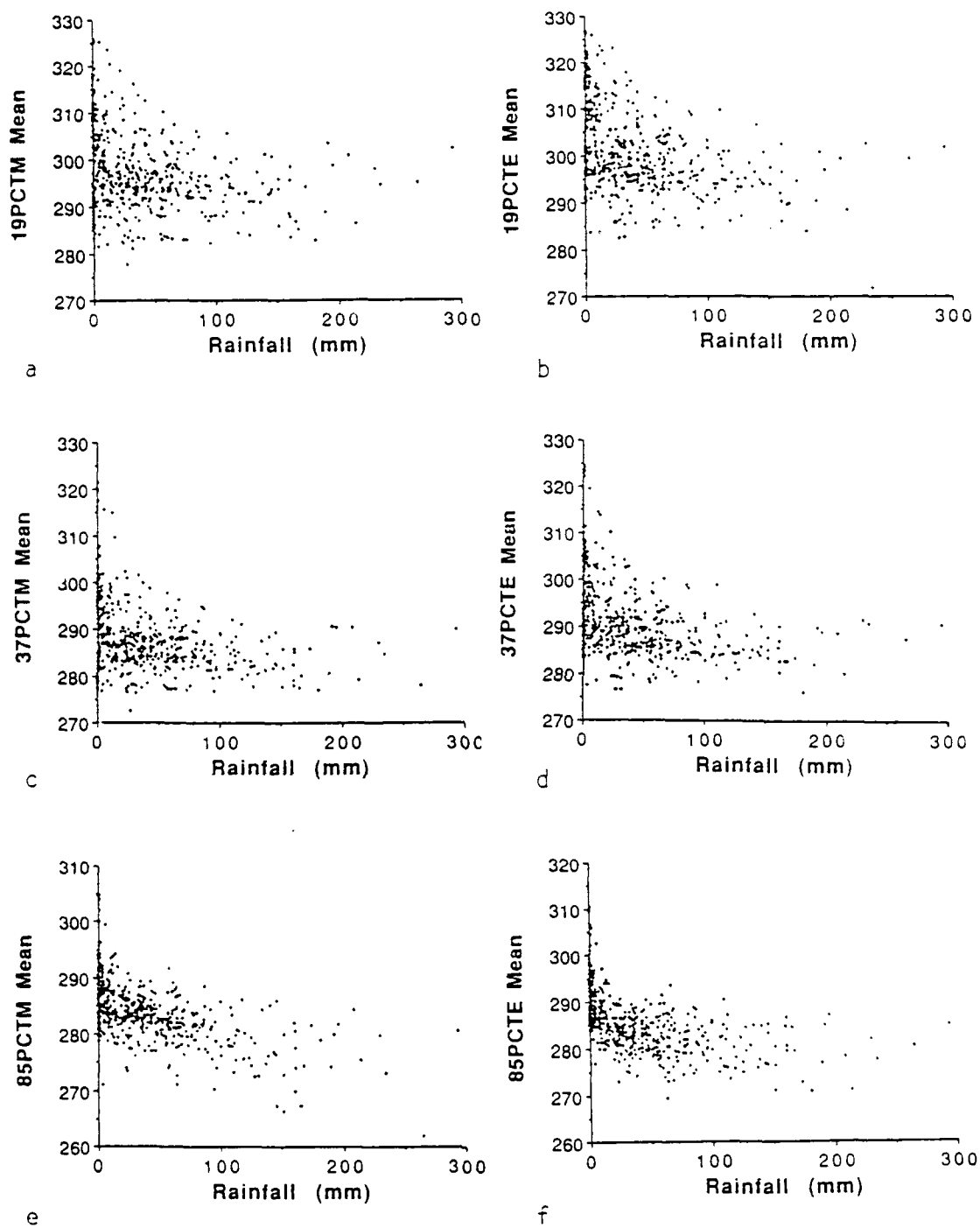


Figure 4.7: Scatter diagrams for a)  $19PCT_M$ , b)  $19PCT_E$ , c)  $37PCT_M$ , d)  $37PCT_E$ , e)  $85PCT_M$ , and f)  $85PCT_E$ .

paper, the difference between 19 GHz and the other three MW frequencies will be called 19/22DIF, 19/37DIF, and 19/85DIF. The scatter diagrams of these parameters are contained in Figure 4.8a-f.

The parameter 19/22DIF, is sensitive to atmospheric water vapor which attenuates emitted radiation from the surface. In addition, 19/22DIF exhibits warming between morning and evening at low rainrates due to surface heating, as did both 19 and 22 GHz. The parameter, 19/22DIF<sub>E</sub>, has the 3rd highest correlation coefficient (-0.632). The range of  $T_B$  for 19/22DIF<sub>E</sub> is +7 to -14, with a slow decrease in  $T_B$  as area-time averaged rainfall increases. The sensitivity of this parameter is about 10 K.

The 19/37DIF parameter is a measure of the difference in surface emissivity and rainfall attenuation of the surface at 19 GHz and the emission and scattering characteristics at 37 GHz. For 19/37DIF, the mean of the PDF of 19 GHz is generally greater than the mean of the PDF at 37 GHz, leading to a mean difference of about 3 K and variance of 9.7 K<sup>2</sup>. Although the data are highly concentrated, they are oriented along a horizontal line. This explains the lower correlation coefficients in Table 4.1 and Figure 4.1.

The last parameter of this type, 19/85DIF, is a measure of the surface emission after the affects of scattering are removed. Based upon the correlation coefficients for this parameter, it does not appear to be well suited as a reliable estimator of subdivisional weekly rainfall. In addition, the scatter diagram for 19/85DIF<sub>M</sub> (Figure 4.8e), shows significant and unorganized scatter thus confirming the parameter's lack of robustness.

The last three parameters are frequency dependent normalized degree of polarizations. These will be referred to as 19NDP, 37 NDP, and 85NDP. All three of

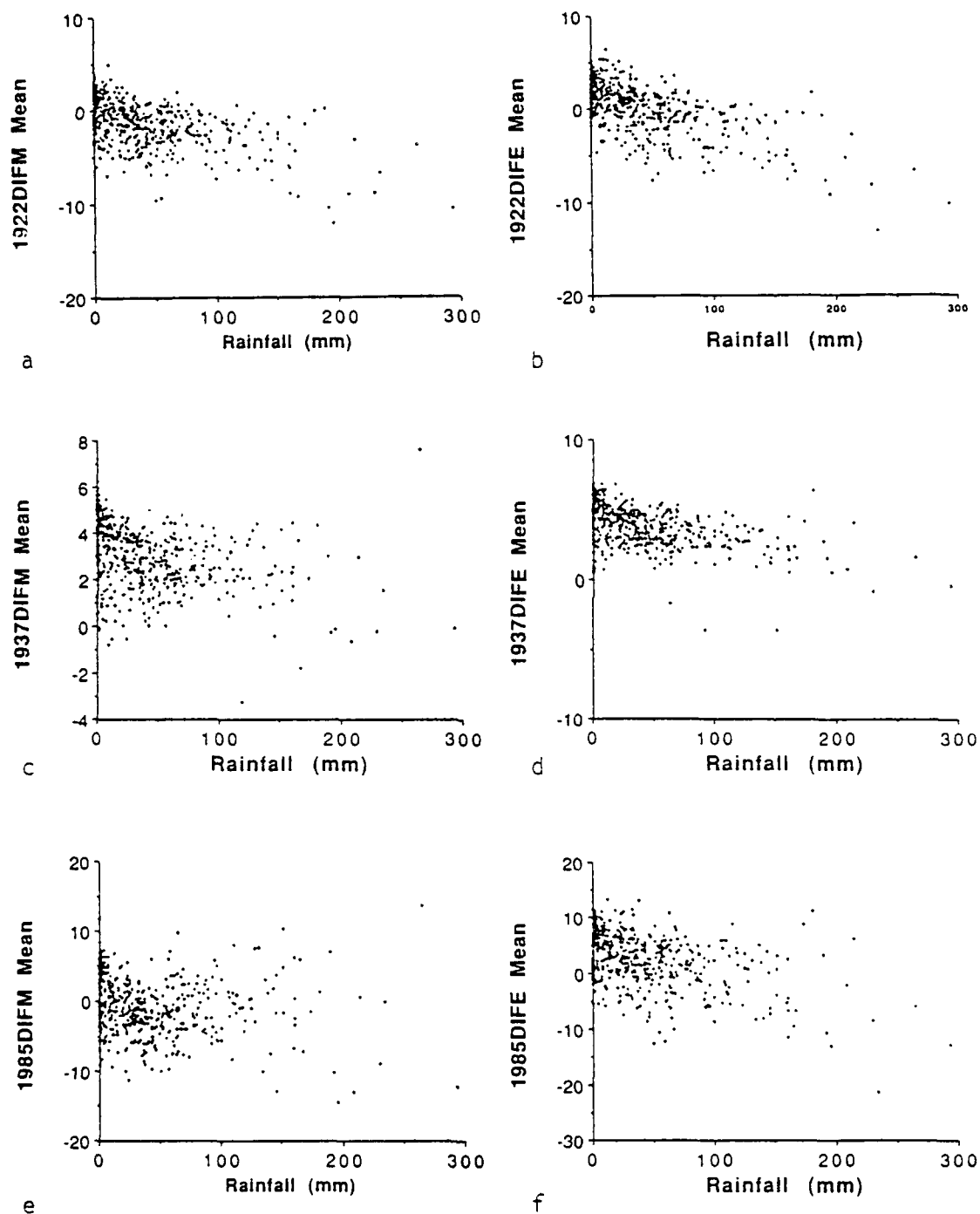


Figure 4.8: Scatter diagrams for a) 19DIF<sub>M</sub>, b) 19DIF<sub>E</sub>, c) 37DIF<sub>M</sub>, d) 37DIF<sub>E</sub>, e) 85DIF<sub>M</sub>, and f) 85DIF<sub>E</sub>.



these parameter means show very low correlation coefficients during both morning and evening orbits and are not robust parameters of subdivisional weekly rainfall.

The standard deviation of the PDF might have a significant correlation with measured weekly subdivisional rainfall based upon the assumption that as rainfall increases, the variances of the  $T_B$  PDFs increase due to the presence of colder  $T_B$ s in FOVs containing rain. A review of the correlation coefficients of the standard deviation of each parameter regressed against weekly rainfall does not generally support this assumption. Table 4.2 shows the results for each parameter for morning and evening orbits during 1988. For most parameters, the correlation coefficients are small with large RMS errors. However  $85H_M$  and  $85U_M$  show correlation coefficients of 0.584 and 0.509, respectively. This suggests that the strong scattering effects at 85 GHz can produce 2nd moment correlation in a PDF. In general, morning orbits have larger correlation coefficients than evening orbits. Also, as rainfall totals increase, the standard deviations also increase, as seen by the generally positive sign of the correlation coefficients.

The next logical step is to investigate whether the addition of the standard deviation to the mean to create a linear two-variable model for each parameter results in a better estimate of the measured subdivisional rainfall. The linear two variable model is given by equation 3.

$$y = a_0 + a_1 * (\text{mean}) + a_2 * (\text{standard deviation}) \quad (3)$$

where  $y$  is the estimated rainfall;  $a_0$  is the model intercept and  $a_1$  and  $a_2$  are the regression coefficients. Once the coefficients are calculated, the estimated rainfall totals are calculated and corrected for negative rainfall. The resulting correlation coefficients for morning and evening orbits are given in Figure 4.9. Correlation coefficients using

Table 4.2: Correlation coefficients and RMS errors for the standard deviation of the 1988 microwave PDFs.

<u>Parameter</u>	<u>Morning Orbits</u>		<u>Evening Orbits</u>	
	R	rms error	R	rms error
19V	0.028	46.73	0.180	45.98
19H	0.079	46.60	0.137	46.30
22V	-0.194	45.86	-0.042	46.71
37V	0.040	46.71	0.075	46.62
37H	0.079	46.60	0.148	46.24
85V	0.287	44.78	0.147	46.24
85H	0.584	37.96	0.236	45.43
19U	0.085	46.58	0.206	45.75
37U	0.094	46.54	0.242	45.36
85U	0.509	40.24	0.229	45.50
19PCT	-0.008	46.74	0.129	46.36
37PCT	0.133	46.33	0.067	46.64
85PCT	0.101	46.51	0.028	46.73
19/22DIF	0.183	45.96	0.264	45.09
19/37DIF	0.180	45.99	0.149	46.23
19/85DIF	0.284	44.83	0.264	45.09
19NDP	0.014	46.74	0.033	46.72
37NDP	0.051	46.69	0.194	45.86
85NDP	-0.126	46.37	-0.119	46.41

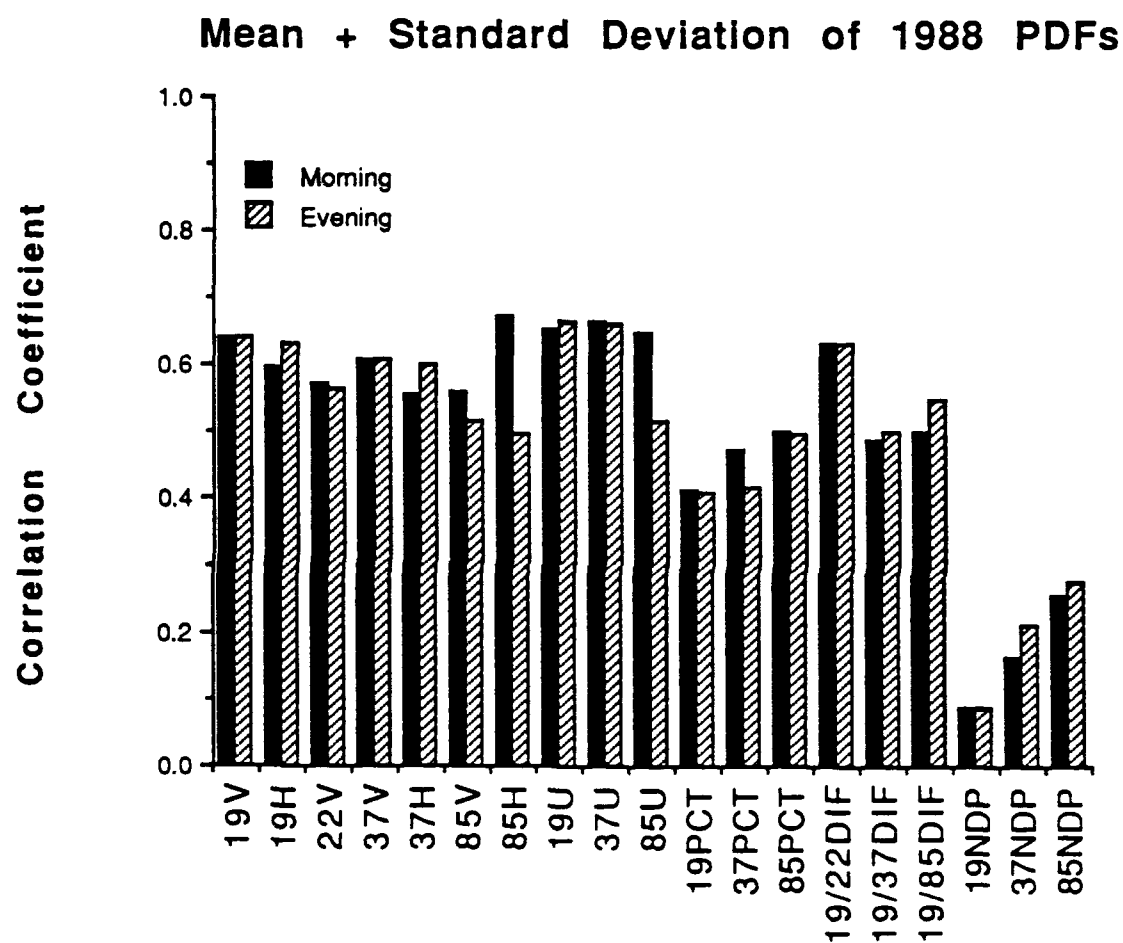


Figure 4.9: Correlation coefficients for the mean + standard deviation of the morning and evening microwave PDFs (1988).

the mean-standard deviation combination generally increase, especially for morning orbits, over correlations using the mean only. In addition, the differences between morning and evening orbits is significantly reduced for most parameters when using the two variable model as compared to the one variable model as shown in Figure 4.10. This is true except for 85H and 85U, which may be due to the large differences in the standard deviations between morning and evening orbits of these parameters. It would be speculative at best to physically explain why the difference between morning and evening parameters decreases when the standard deviation is added to the model.

**4.1.2 Properties of the infrared probability distribution functions.** The mean of the IR PDFs represent the time-area averaged cloud-top temperature, or under cloud-free conditions, the surface skin temperature attenuated by the overlying atmosphere. The means of the IR PDFs for 1988 are independently evaluated following the methods in section 2.3. Rainfall retrieval algorithms based upon IR measurements, unlike MW measurements, provide an indirect estimate of rainfall because these measurements are only able to detect cloud top temperatures and cannot penetrate through cloud layers. In addition, different cloud types can have similar temperatures but far different surface weather conditions. For example, high, dense cirrus may have the same cloud-top temperature as a cumulonimbus, however, dry surface conditions prevail under the cirrus while heavy rainfall occurs under the cumulonimbus.

The results of the IR analysis are compiled in Table 4.3. Correlation coefficients of the mean of the IR PDFs are high when compared against the mean of the PDFs of most MW parameters. Only a few of the evening MW parameters have correlation coefficients that approach those of the IR correlation coefficients. In addition, the IR correlation coefficients appear to be out of phase with the MW correlation coefficients.

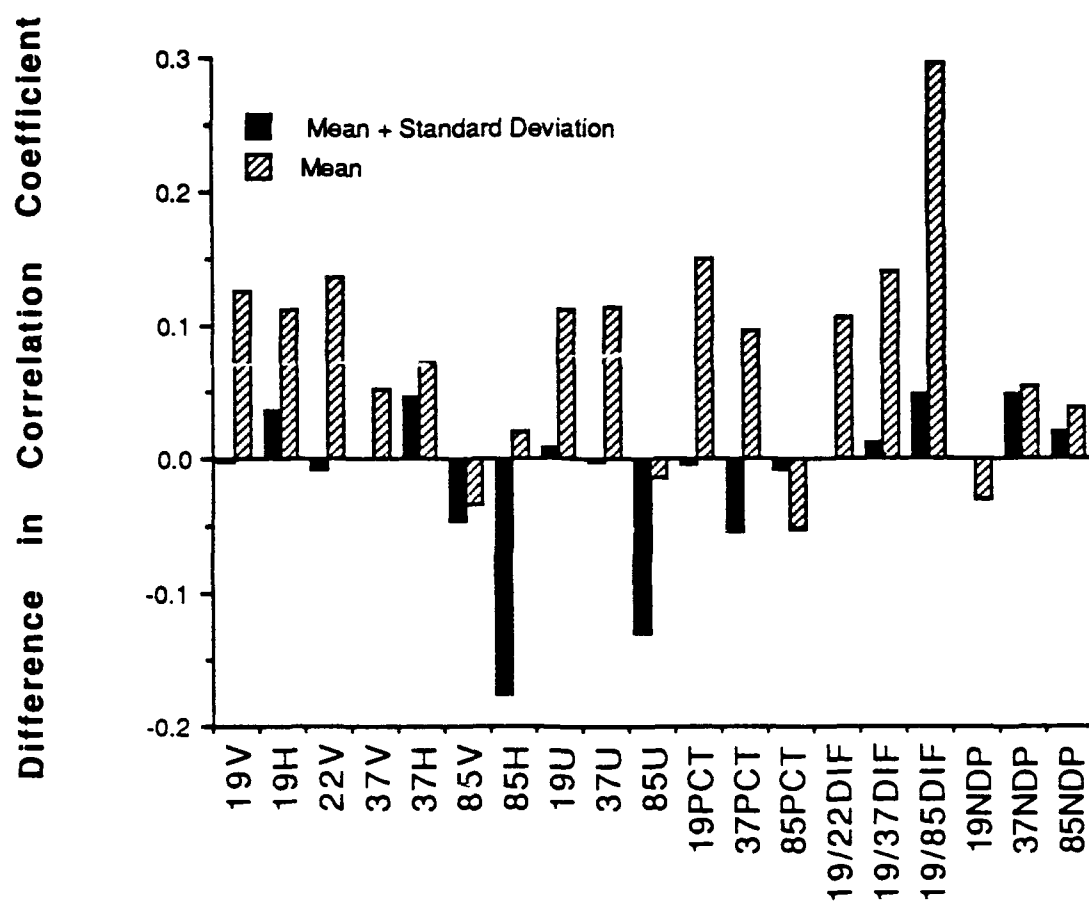


Figure 4.10: Difference between evening and morning correlation coefficients for the mean + standard deviation of the PDFs (1988).

Table 4.3: Correlation coefficients and RMS errors for the mean of the 1988 IR PDFs.

<u>GMT</u>	<u>MST</u>	<u>Correlation Coefficient</u>	<u>RMS error</u>
0000	0530	-0.7140	32.73
0300	0830	-0.7217	32.36
0600	1130	-0.6856	34.03
0900	1430	-0.6212	34.63
1200	1730	-0.5624	38.65
1500	2030	-0.5534	38.94
1800	2330	-0.6100	37.04
2100	0230	-0.6710	34.66

The mean of the morning IR PDFs have high correlation coefficients while the mean of the morning MW PDFs have low correlations, and vice versa in the evening. Figure 4.11, show that a pronounced diurnal cycle in the correlation exists using the mean of the IR PDFs.

Studies have shown that the preferred period of thunderstorm occurrence, in India, is during the night with maximum occurrence during the early and late evening and a secondary maximum in the afternoon (Sivarmakrishnan, 1990). Thunderstorm activity is at a minimum in the morning. It should be noted that significant departures from the general diurnal cycle occurs near coastal regions and elevated topography. Based upon this, it would seem that the high morning IR correlations are erroneous. This can be explained by understanding that the IR measures only cloud top temperatures and not rainfall. For example, when thunderstorm activity begins to increase throughout the afternoon, cirrus anvil debris is generated, thus contaminating the FOVs with non-raining clouds having low temperatures. In contrast, the mean of MW parameter PDFs have generally higher correlations than the mean of IR PDFs during the evening because at MW frequencies, cirrus clouds are essentially transparent. Thus only the raining cloud and the underlying surface affect the MW measurements.

**4.1.3 Properties of microwave cumulative distribution functions.** The properties of the MW CDFs investigated include the slope and intercept factors. The slope factor represents behavior in the tail of the CDF under varying rain conditions. For example, as rainfall increases, the slope should decrease due to colder  $T_B$  being present within the CDF. The intercept factor as used here represents the coldest  $T_B$  found within a subdivision for a given week and may not be representative of overall

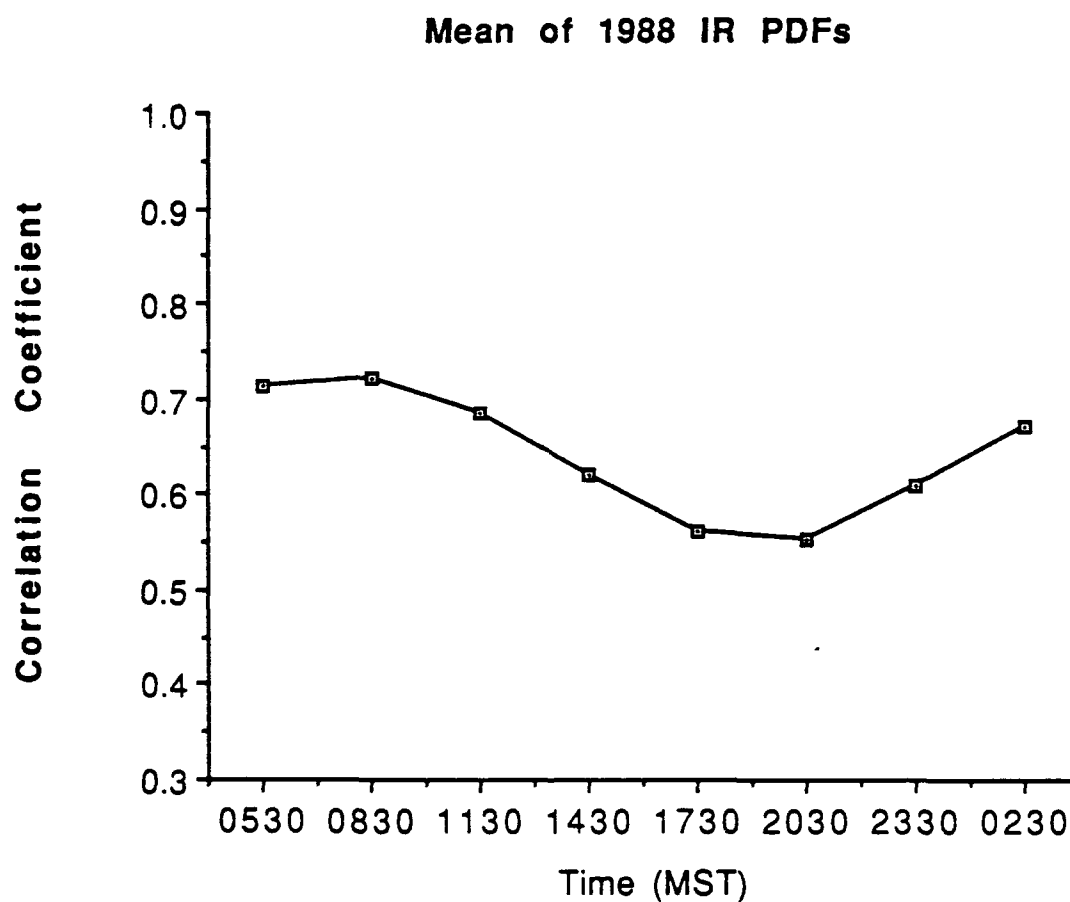


Figure 4.11: Diurnal cycle of cloudiness as seen in the fluctuations of IR correlation coefficients.



conditions during the week. Other definitions of the intercept factor are possible and may return better results, however, they were not investigated in this study.

A linear least squares fit of the slope factor to measured rainfall is calculated in the same manner as used for the PDF analysis. The correlation coefficients and RMS error for the morning orbits and evening orbits are compiled in Table 4.4. An examination of these figures reveals that the slope factor of the CDF is not a robust variable to be used as an estimator of subdivisional rainfall. The highest correlation at any frequency is -0.331 for  $85H_M$ .

An analysis of the intercept factor of the CDF reveals that it is not a robust variable. Table 4.5 list the correlation coefficients and the mean square errors for the morning and evening orbits. The most effective frequency for subdivisional rainfall detection is again  $85H_M$  with a correlation coefficient of almost -0.382.

## 4.2 Multi-parameter Regression Analysis

Although a correlation coefficient of -0.659 using the mean of the  $37U_E$  PDF is respectable for estimating rainfall over land from MW measurements, improvements are possible by using a multi-parameter regression model based upon the mean. All 38 MW parameters are entered into a multiple linear regression model which selects the optimal regression model for each subset of parameters for use in 1987. The 85 GHz vertical channel malfunctioned in 1989, therefore 28 parameters are used in a multiple linear regression program to obtain the optimal model, WO85V, for use in 1989. A Regression Model Correlation Function (RMCF) is generated to describe model behavior by obtaining the correlation coefficient after new parameters are sequentially added to the model.

Table 4.4: Correlation coefficients for the slope factor of the 1988 microwave CDFs.

<u>Parameter</u>	<u>Morning Orbits</u>		<u>Evening Orbits</u>	
	R	rms error	R	rms error
19V	-0.081	46.59	-0.060	46.66
19H	-0.184	45.95	-0.196	45.84
22V	0.240	45.38	0.241	45.37
37V	-0.064	46.65	0.006	46.75
37H	-0.103	46.50	-0.083	46.58
85V	-0.169	46.08	-0.127	46.37
85H	-0.331	44.11	-0.187	45.92

Table 4.5: Correlation coefficients for the intercept factor of the 1988 microwave CDFs.

<u>Parameter</u>	<u>Morning Orbits</u>		<u>Evening Orbits</u>	
	R	rms error	R	rms error
19V	-0.096	46.53	-0.147	46.24
19H	-0.034	46.72	-0.055	46.67
22V	0.124	46.39	0.026	46.73
37V	-0.046	46.70	0.003	46.75
37H	0.019	46.74	-0.003	46.75
85V	-0.121	46.40	-0.082	46.59
85H	-0.382	43.20	-0.142	46.28

**4.2.1 Model building with microwave parameters.** The RMCF of the optimal 1988 multi-parameter regression model is shown in Figure 4.12. The correlation coefficient reaches a limit near -0.80, beyond which the addition of MW parameters to the optimal model yields little information with which to predict the measured subdivisional rainfall. Table 4.6 lists the MW parameters used in the optimal regression model up to 8 variables, along with correlation coefficients and RMS errors.

Interestingly, some of the parameters that appear in the optimal models are not individually robust. For example, the two-parameter optimal model contains  $37U_E$  and  $19/85DIF_M$ . From Table 4.1, the correlation coefficient of  $19/85DIF_M$  has a correlation coefficient of -0.149, but in the two-parameter model it is more important than any of the remaining 36 parameters. It is difficult to say why  $19/85DIF_M$  entered the model at this point, however, it is instructive to examine the top five optimal two-parameter models. Four of the top five contained  $37U_E$  and some form of a morning 85.GHz parameter ( $19/85DIF_M$ ,  $85PCT_M$ ,  $85V_M$ , and  $85U_M$ ). Therefore, information concerning the scattering measured during the morning at 85 GHz appears to be important and should be included in any regression model used to estimate area-time averaged rainfall over land.

An optimal model containing three parameters adds, in addition to the terms from the two-parameter model,  $19/22DIF_M$  and increases the correlation coefficient to 0.736 and reduces the RMS error to 31.62 mm. This term provides information concerning the attenuation by water vapor of the surface emission. Individually,  $19/22DIF_M$  and  $19/22DIF_E$  have high correlations with rainfall of -0.525 and -0.623, respectively. Based upon its early entry into the regression model and its high correlation with measured rainfall, it is clear that this is a robust parameter to use to observe area-time averaged rainfall over land regions. In the optimal three-parameter

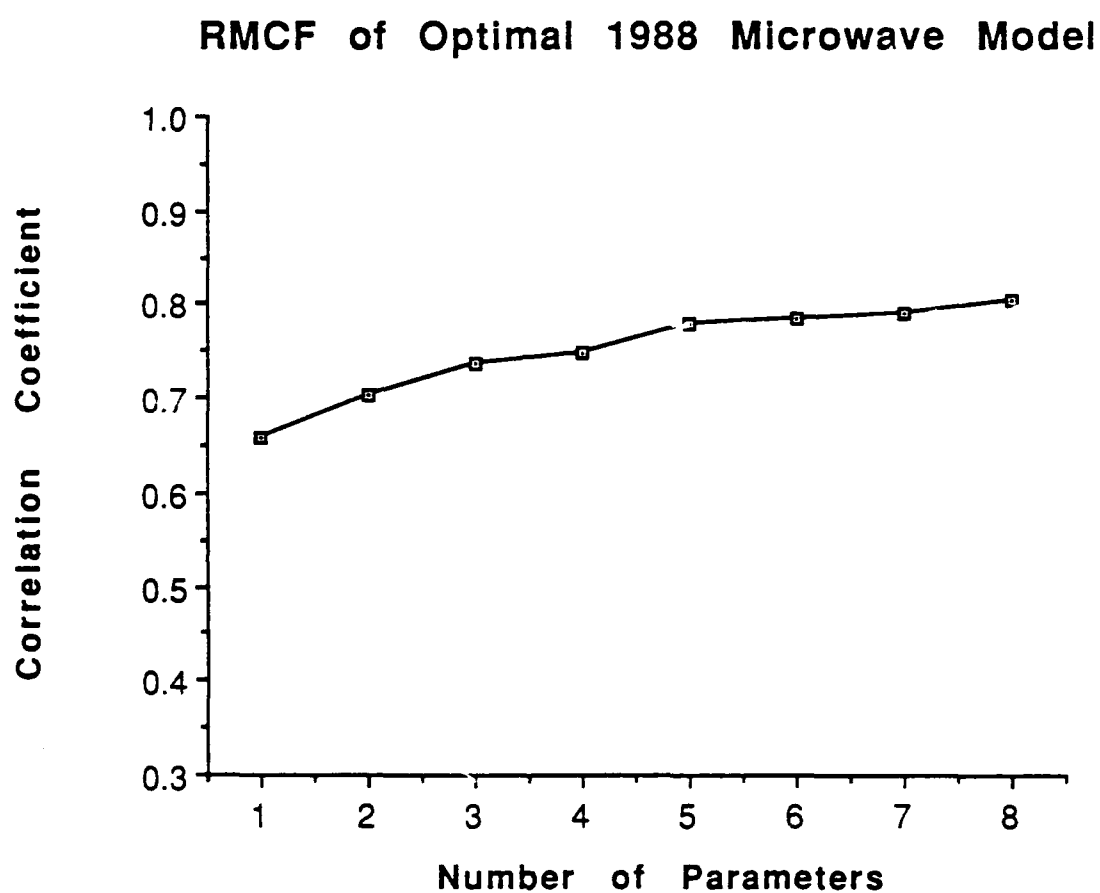


Figure 4.12: Regression Model Correlation Function (RMCF) for optimal multi-parameter model based upon the mean of the 1988 PDFs.

Table 4.6: Parameters used in optimal regression model along with correlation coefficients and RMS errors at each step.

Parameter	R	rms error
$^{37}\text{U}_\text{E}$	-0.659	35.12
$^{19}/^{85}\text{DIF}_\text{M}$	-0.704	33.18
$^{19}/^{22}\text{DIF}_\text{M}$	-0.736	31.62
$^{85}\text{PCT}_\text{E}$	-0.749	30.97
$^{19}\text{PCT}_\text{M}$	-0.779	29.28
$^{19}\text{PCT}_\text{E}$	-0.786	28.89
$^{85}\text{V}_\text{E}$	-0.791	28.60
$^{85}\text{NDP}_\text{M}$	-0.804	27.79

model, another trend is noticeable in the top five parameter candidates for inclusion into the model. Each of the candidate parameters is a form of the 19 GHz channel ( $19DIF_M$ ,  $19/37DIF_M$ ,  $19/22DIF_E$ ,  $19NDP_M$ , and  $19H_M$ ). In addition, the top three are differential  $T_B$  at vertical polarizations of the lower frequencies. Therefore, it appears that the surface and rain-layer emission and degree of water vapor absorption variability is taken into account with the addition of these parameters. Moreover, when additional parameters are added to the optimal model, it appears that the key physical radiative processes (surface and rain-layer emission, within cloud volume scattering, water vapor absorption variability, and polarization differences) are accounted for.

When a combination of the mean and standard deviation are used in a multi-parameter regression model, results similar to that of models using only the mean are obtained. Figure 4.13 shows the RMCF of the optimal mean-standard deviation multi-parameter regression models for the first 8 parameters. The combination mean-standard deviation have slightly higher correlation coefficients than the mean-only models, however, the difference is insignificant. The primary difference between the two approaches is the subset of parameters that are chosen in each optimal regression model. Only three of the parameters are common to both approaches;  $19/22DIF_M$ ,  $85PCT_E$ , and  $19/85DIF_M$ . Table 4.7 lists the parameters used in the first 8 regression subsets, along with correlation coefficients and the RMS model errors.

**4.2.2 Model building without 85V GHz parameters.** Table 4.8 lists the best parameters, without 85V parameters (WO85V), at each step through an 8 parameter regression model. An interesting feature of this model is that with the exception of  $37U_E$ , when fewer than five parameters are used, only SSM/I frequencies appear. Also, the correlation coefficients of the WO85V model, are approximately 5 percent less than

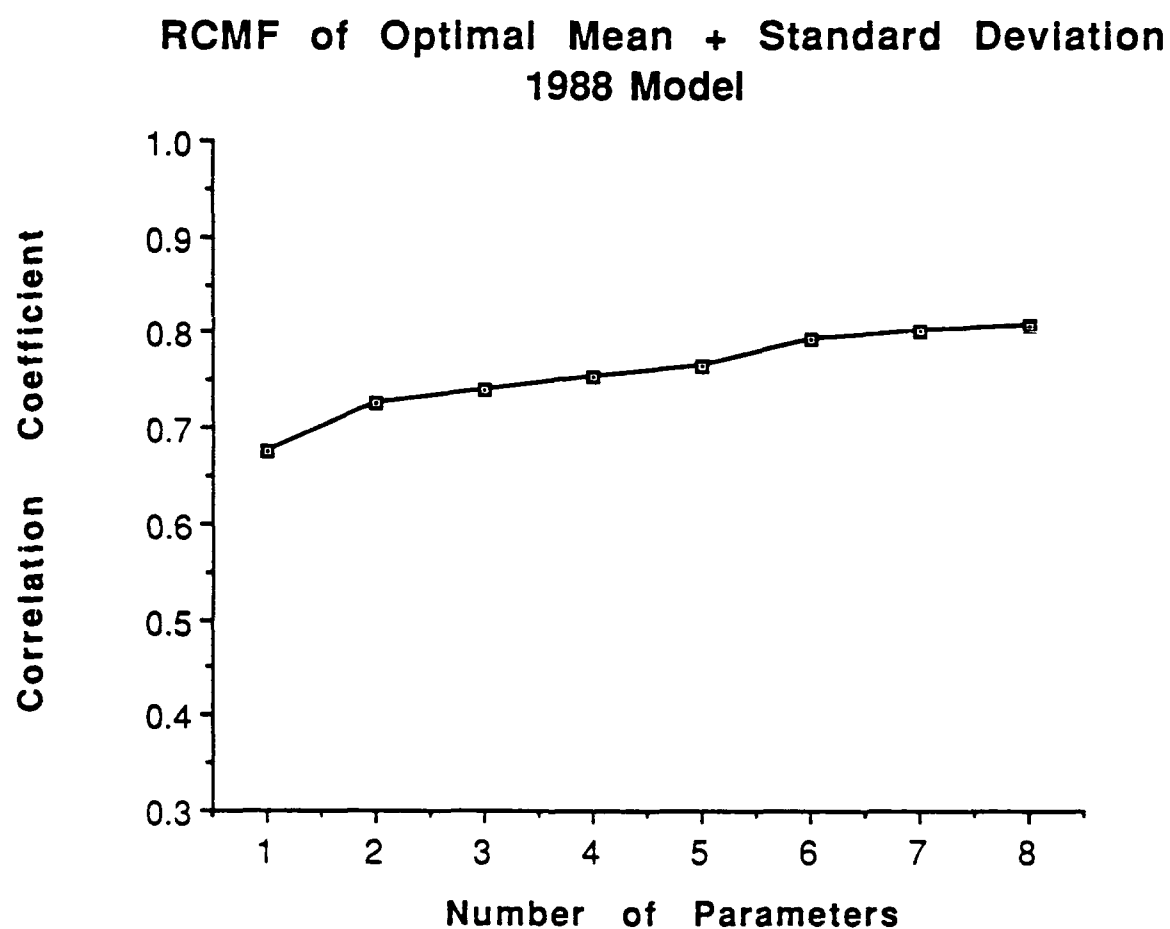


Figure 4.13: RCMF for optimal multi-parameter model based upon the mean + standard deviation of the 1988 PDFs.

Table 4.7: Mean + standard deviation regression model parameters with correlation coefficients and RMS errors.

Parameter	R	rms error
$^{19}\text{U}_{\text{E}}$	-0.676	34.45
$^{85}\text{H}_{\text{M}}$	-0.725	32.14
$^{37}\text{U}_{\text{M}}$	-0.740	31.42
$^{19}/^{22}\text{DIF}_{\text{M}}$	-0.754	30.69
$^{85}\text{PCT}_{\text{E}}$	-0.763	30.16
$^{19}\text{V}_{\text{M}}$	-0.794	28.40
$^{85}\text{H}_{\text{E}}$	-0.801	28.03
$^{19}/^{85}\text{DIF}_{\text{M}}$	-0.807	27.94



Table 4.8: WO85V multi-parameter regression model parameters correlation coefficients and RMS errors.

Parameter	R
$37U_E$	-0.659
$22V_M$	-0.677
$19V_E$	-0.706
$85H_M$	-0.739
$37H_E$	-0.747
$19NDP_E$	-0.760
$37PCT_E$	-0.767
$19PCT_M$	-0.777

the optimal 1988 model. The small difference is probably due to the high degree of correlation between some parameters.

In the WO85V two-parameter model,  $22V_M$  enters into the model following 37UE, however only a marginal increase in correlation occurs (0.018). Of interest, is that in both this model and the full parameter models, a form of 22 GHz (19/22DIF) enters into the regression very quickly. These parameters provide the model with information concerning the average water vapor content of the atmosphere within a subdivision.

In the WO85V three-parameter model,  $19V_E$  enters the model, as a form of 19 GHz did in the models containing the 85V parameters. This and the fact that a form of 22 GHz appears in the optimal and WO85V regression models emphasize the importance of these emission-based parameters. Until now, these parameters were of little use in the detection of rainfall over land due to the size of the FOVs and associated beam-filling errors. However, in this study the beam-filling errors have been reduced by deconvolving the MW measurements to the higher spatial resolution of the 85 GHz channels. Therefore, a higher degree of sensitivity to rainfall over land can be attained by using deconvolved low frequency MW measurements. Again, as the number of parameters in the WO85V model increases, the key physical radiative processes are accounted for. However, the parameters accounting for volume scattering are based upon 37 GHz instead of 85 GHz.

**4.2.3 Model building with microwave and IR parameters.** Before a mixed IR-MW multi-parameter regression model is created, an IR-only multi-parameter model is examined using all eight of the daily measurements that are available in 1988. As shown in section 4.1.2, the 0300 GMT measurements have the highest correlation (-0.721) with measured subdivisional rainfall than any other IR measurement times. However, a multiple regression of the means of the IR PDFs for the eight times they are available

shows that the highest correlation (-0.738) occurs after four parameters (0300, 0900, 1500, and 2100 GMT) are entered into the model and then decreases as more parameters are added. Based upon this, it is apparent that only one IR parameter is needed in a mixed IR-MW optimal regression model due to the high correlations between IR measurements. This was verified by using all eight IR parameters plus the 38 MW parameters in a multiple linear regression program to obtain the best mixed IR-MW regression model.

Section 4.1.2 shows that some morning IR parameters have higher correlation coefficients than any of the MW parameters. An optimal IR-MW multi-parameter regression model was obtained which shows that a mixed model can be constructed which uses fewer parameters to attain the same performance level of MW models. Also, as the number of parameters increase, a limit is again approached nearly equal to that of the MW-only models. Figure 4.14 shows the RMCf based upon 0600 GMT IR measurements in combination with MW parameters.

The optimal IR-MW models containing either 0000, 0300, 0600, or 2100 GMT IR measurements all contained the same additional MW parameters. In addition, these parameters all entered into the model in the same order. Table 4.9 lists the first 8 parameters based upon a optimal 0600 GMT IR-MW model. Individually, the remaining IR measurements have correlation coefficients less than some evening MW parameters and therefore do not enter the optimal IR-MW model until the third parameter.

Of interest, are the type of MW parameters which enter the optimal IR-MW regression model. The second parameter to enter is  $19/22DIF_E$ , albeit evening, it is the same parameter which enters the optimal MW regression models. In addition, the next two parameters are differential  $T_B$  at vertical polarizations ( $19/85DIF_M$  and  $19/85DIF_E$ ).

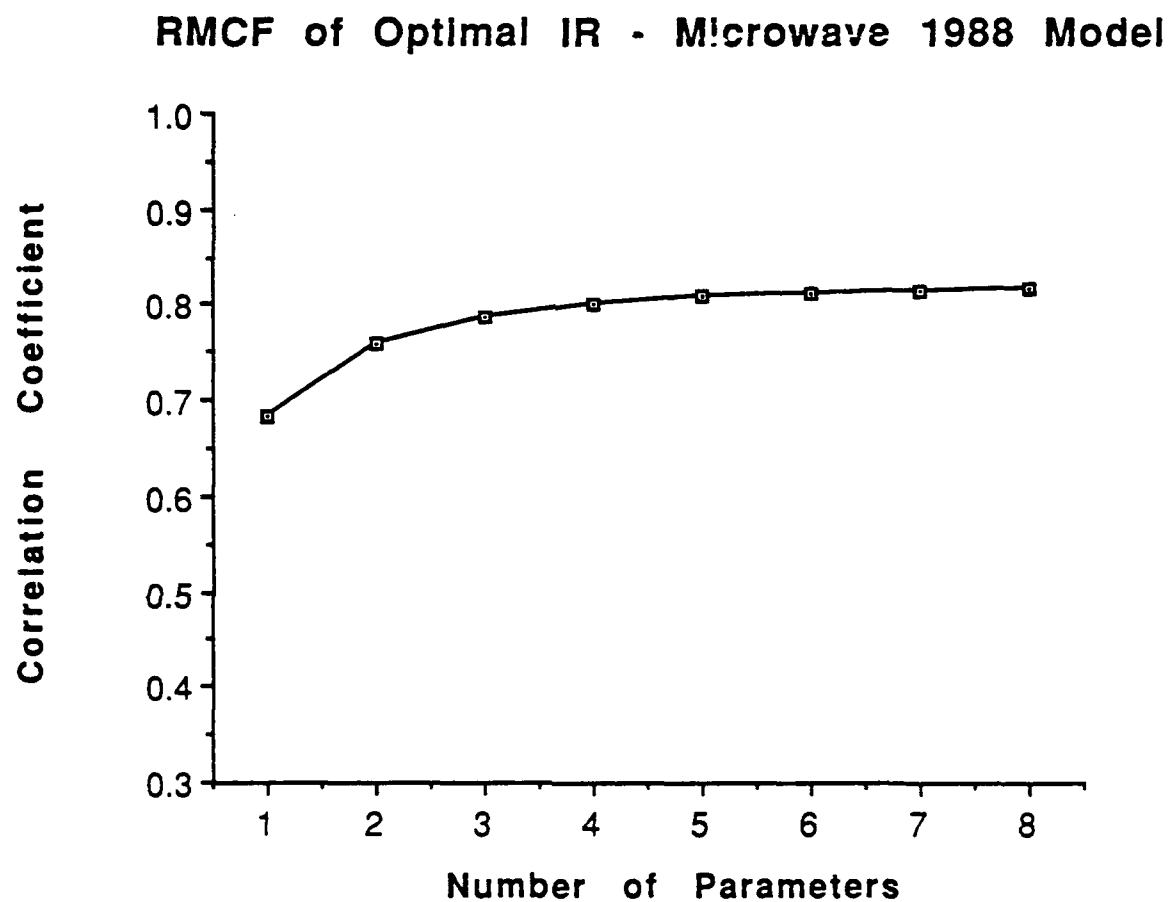


Figure 4.14: RMCF of optimal IR-microwave model based upon the mean of the 1988 PDFs.

Table 4.9: IR-microwave optimal regression model parameters with the correlation coefficients and RMS errors.

Parameter	R	rms error
INSAT 06 GMT	-0.685	34.03
19/22DIF <sub>E</sub>	-0.759	32.14
19/85DIF <sub>M</sub>	-0.789	31.42
19V <sub>M</sub>	-0.800	30.69
19/85DIF <sub>E</sub>	-0.811	30.16
85NDP <sub>M</sub>	-0.812	28.40
85NDP <sub>E</sub>	-0.816	28.03
19/22DIF <sub>M</sub>	-0.818	27.94

## CHAPTER 5

### Validation Tests

Verification of the results obtained for the 1988 monsoon season is accomplished by testing against results obtained from the monsoon seasons of 1987 and 1989. Validation will be performed for the single and optimal (WO85V) 1988 multi-parameter models using the mean of the 1987 (1989) MW PDFs.

#### 5.1 1987 Tests

Figure 5.1 illustrates the variation between individual parameters in terms of correlation coefficients for morning and evening orbits. Table 5.1 lists the individual parameter correlation coefficients and RMS errors. An interesting result, is that during 1987 the mean of the morning MW parameters have higher correlation coefficients than their evening counterparts. This is the opposite of the results obtained for the 1988 MW parameters. In particular, during 1987,  $85PCT_M$  has the highest correlation coefficient (-0.601); during 1988,  $85PCT_M$  has a correlation of -0.540 and was one of the few parameters which had a higher correlation in the morning than it did in the evening. This may be due to the evening 85PCTs being adversely affected by high surface

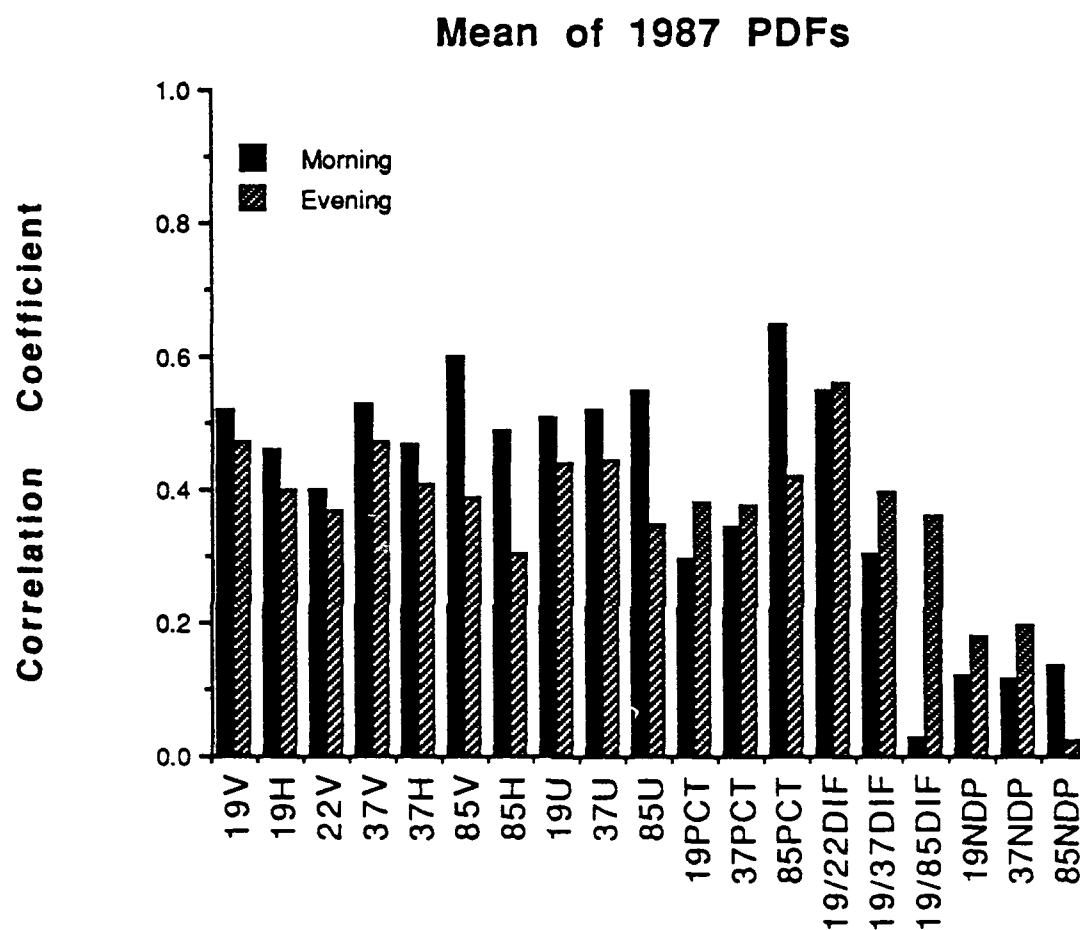


Figure 5.1: Correlation coefficients of the mean of the 1987 morning and evening PDFs.

Table 5.1: Parameter correlation coefficients and RMS errors for 1987.

Parameter	Morning		Evening	
	Correlation	RMSE	Correlation	RMSE
19V	-0.512	36.06	-0.468	34.32
19H	-0.461	39.16	-0.400	40.66
22V	-0.398	40.44	-0.374	41.31
37V	-0.520	37.45	-0.468	39.22
37H	-0.470	38.96	-0.403	40.60
85V	-0.598	35.25	-0.395	41.00
85H	-0.486	38.54	-0.312	42.36
19U	-0.508	37.96	-0.436	39.95
37U	-0.520	37.66	-0.439	39.87
85U	-0.549	36.85	-0.356	41.69
19PCT	-0.298	42.11	-0.374	41.15
37PCT	-0.342	41.42	-0.364	41.18
85PCT	-0.631	33.63	-0.423	40.37
19/22DIF	-0.547	36.89	-0.551	36.80
19/37DIF	-0.306	42.00	-0.389	40.85
19/85DIF	-0.029	44.10	-0.348	41.48
19NDP	0.120	43.80	0.178	43.74
37NDP	0.117	43.81	0.192	43.59
85NDP	-0.136	43.70	-0.021	44.44



temperatures. Both  $19/22DIF_M$  and  $19/22DIF_E$  have high correlation coefficients, similar in magnitude to those of 1988.

The differences between 1987 and 1989 may be related to a shift in the diurnal rainfall cycle based upon the following observations. A comparison of Tables 5.1 and 4.1 reveals that the difference between MW parameters during morning orbits is small. However, the difference between the same parameters during the evening is much larger. Because these correlations are between the means of parameter PDFs and weekly rainfall totals, fluctuation in the correlation coefficients may be indicative of a shift in the diurnal rainfall pattern.

Figure 5.2 illustrates how the RMCF based upon the optimal MW 1988 multi-parameter model applied to 1987 data. As the the number of parameters increase, the correlation coefficient does not always increase. This is, in part, due to the optimal 1988 parameters not being as robust during 1987. For example, all of the 1988 optimal multi-parameter models are based upon  $37U_E$  since it has the highest individual correlation coefficient of any MW parameter. However, in 1987,  $37U_E$  ranks 15 out of 38 MW parameters. Since the optimal 1988 models are based upon  $37U_E$ , it is not surprising that they do not perform as well in 1987.

To investigate which parameters might work best in a independent multi-parameter model for 1987, a model was constructed using only as input the 1987 MW measurements by the procedure in section 4.2.1. Figure 5.2 also shows the behavior of the RMCF of the 1987 independent MW multi-parameter model. In the independent 1987 multi-parameter regression model,  $85PCT_M$  forms the basis of the model since, individually it has the highest correlation with subdivisional rainfall. The second and third parameters added are  $37PCT_M$  and  $19/22DIF_M$ , respectively (Table 5.2). Only with the early inclusion of  $19/22DIF_M$ , do the 1987 and 1988 optimal multi-parameter

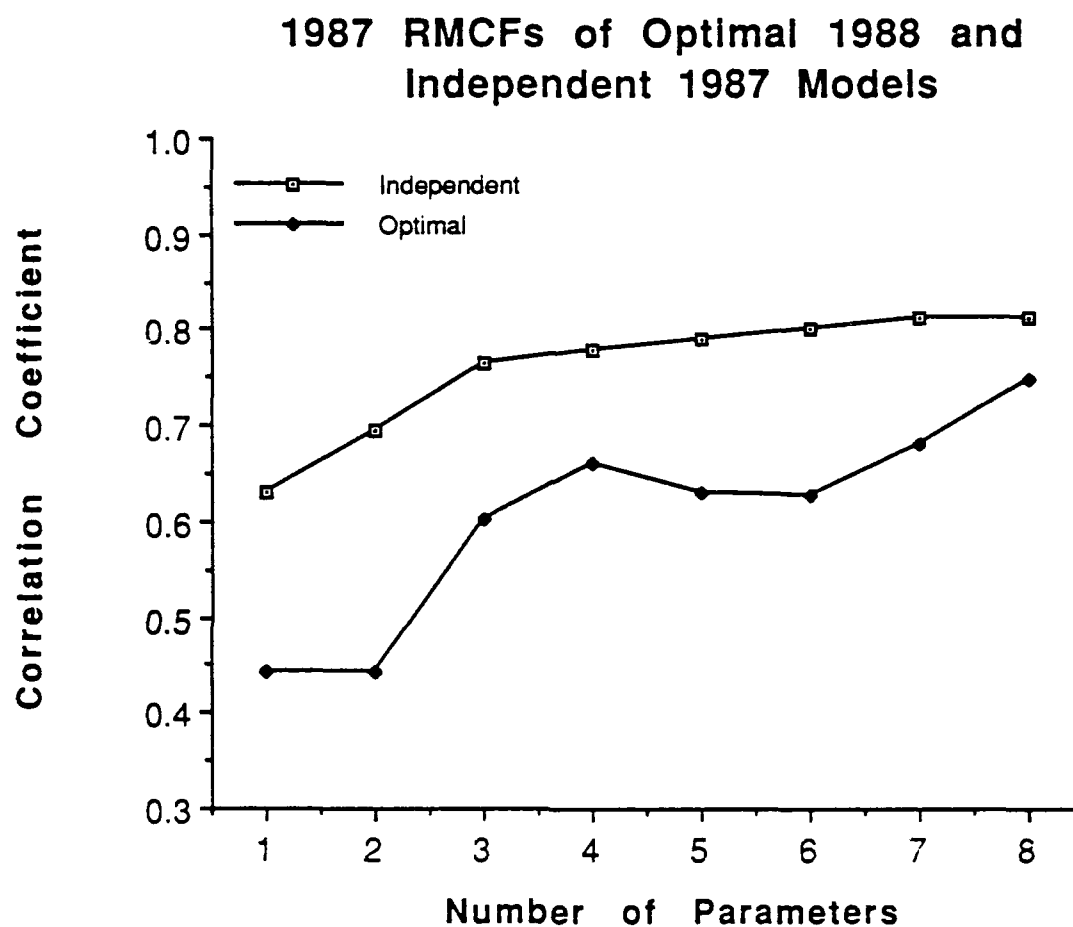


Figure 5.2: RMCFs of the Optimal 1988 microwave multi-parameter model applied to 1987 data and the independent 1987 multi-parameter model.

Table 5.2: Parameters used in independent 1987 regression model along with correlation coefficients.

Parameter	R
$85\text{PCT}_M$	-0.630
$37\text{PCT}_M$	-0.695
$19/22\text{DIF}_M$	-0.764
$37\text{NDP}_E$	-0.780
$85\text{PCT}_E$	-0.789
$19/22\text{DIF}_E$	-0.800
$37\text{V}_E$	-0.813
$37\text{U}_M$	-0.815

models share anything in common. In addition, the 1988 optimal model applied to 1987 and the independent model have a difference of 7.5% after eight parameters are entered into the model. This occurs as the number of parameters increases, when the two models contain many of the same class of parameters. Therefore, the key physical radiative processes are accounted for in the 1987 independent model.

## 5.2 1989 Tests

Figure 5.3 illustrates the variation among individual MW parameters in terms of correlation coefficients for morning and evening parameters. In 1989, like 1988, the evening parameters have higher correlation coefficients than their morning counterparts. Table 5.3 lists the correlation coefficients and RMS errors of the 1989 data.

During 1989,  $19V_E$  and  $37V_E$  tied for the highest correlation coefficients (-0.545), although  $19V_E$  falls short of the results of 1988. However, based upon this, it appears that these two parameters are able to detect time-area averaged rainfall over land in a heavy rainfall regime. A number of parameters have correlations in excess of -0.5 and include  $37V_E$ ,  $37H_E$ ,  $19U_E$ , and  $19/22DIF_E$ ; no morning parameters exceed a correlation of -0.5. The RMS errors range from 34.32 to 40.91 millimeters and the average rainfall during the year is 34.15 millimeters.

The RMCF decreases as the number of parameters in the model exceed three when using the WO85V regression model as seen in Figure 5.4. To gain insight on why this happens, an independent multi-parameter regression model based upon 1989 data is constructed. For this case, the RMCF increases as parameters are added to the model as seen in Figure 5.4. The parameters chosen in the independent 1989 model (Table 5.4) are different than those selected in 1988. In 1989,  $37U_E$  formed the basis of the

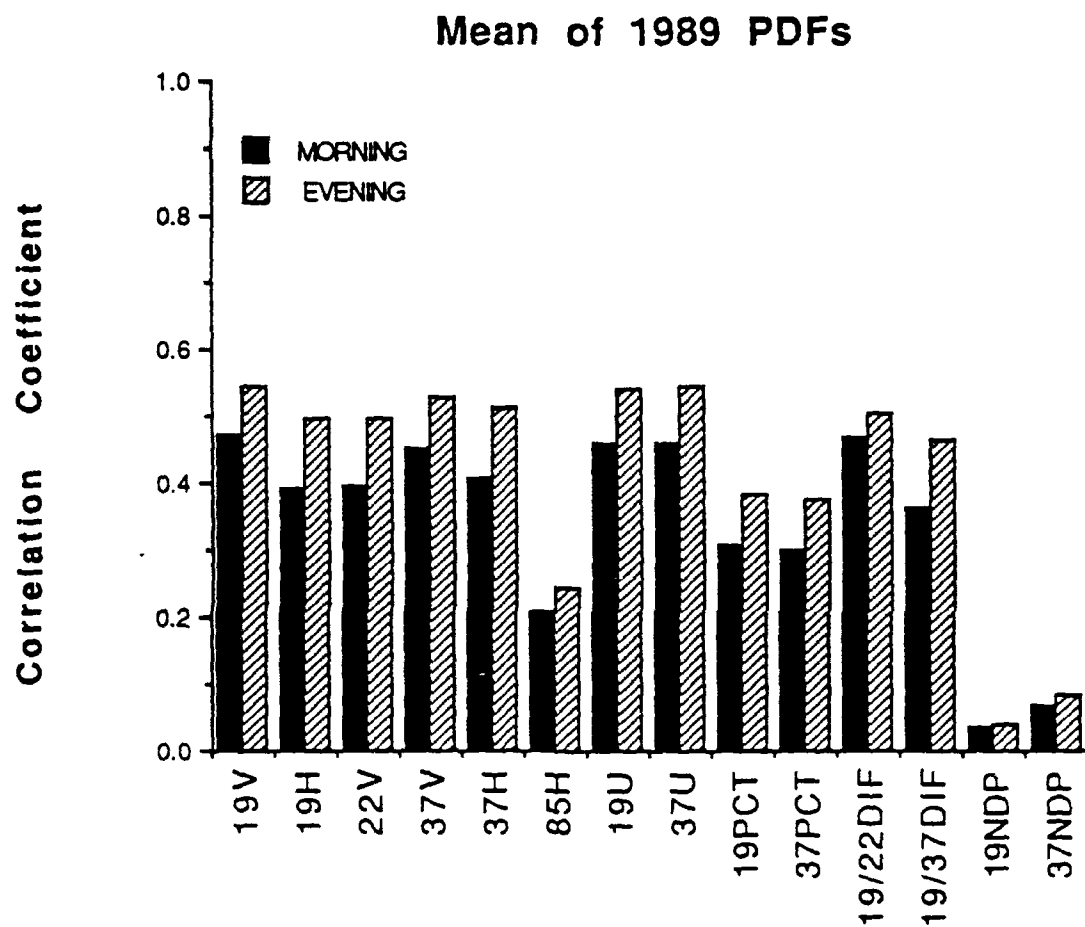


Figure 5.3: Correlation coefficients of the mean of the 1989 morning and evening PDFs.

Table 5.3: Parameter correlation coefficients and RMS errors for 1989.

Parameter	Morning		Evening	
	Correlation	RMSE	Correlation	RMSE
19V	-0.465	36.06	-0.527	34.32
19H	-0.394	37.63	-0.494	35.57
22V	-0.389	37.61	-0.475	35.58
37V	-0.445	36.50	-0.509	34.80
37H	-0.406	37.41	-0.512	35.13
85H	-0.209	40.04	-0.247	39.72
19U	-0.456	36.39	-0.535	34.40
37U	-0.456	36.38	-0.536	34.83
19PCT	-0.308	38.94	-0.383	37.78
37PCT	-0.296	39.05	-0.367	37.94
19/22DIF	-0.469	36.14	-0.505	35.31
19/37DIF	-0.363	38.15	-0.461	36.29
19NDP	-0.036	40.91	0.038	40.91
37NDP	-0.069	40.84	0.084	40.79

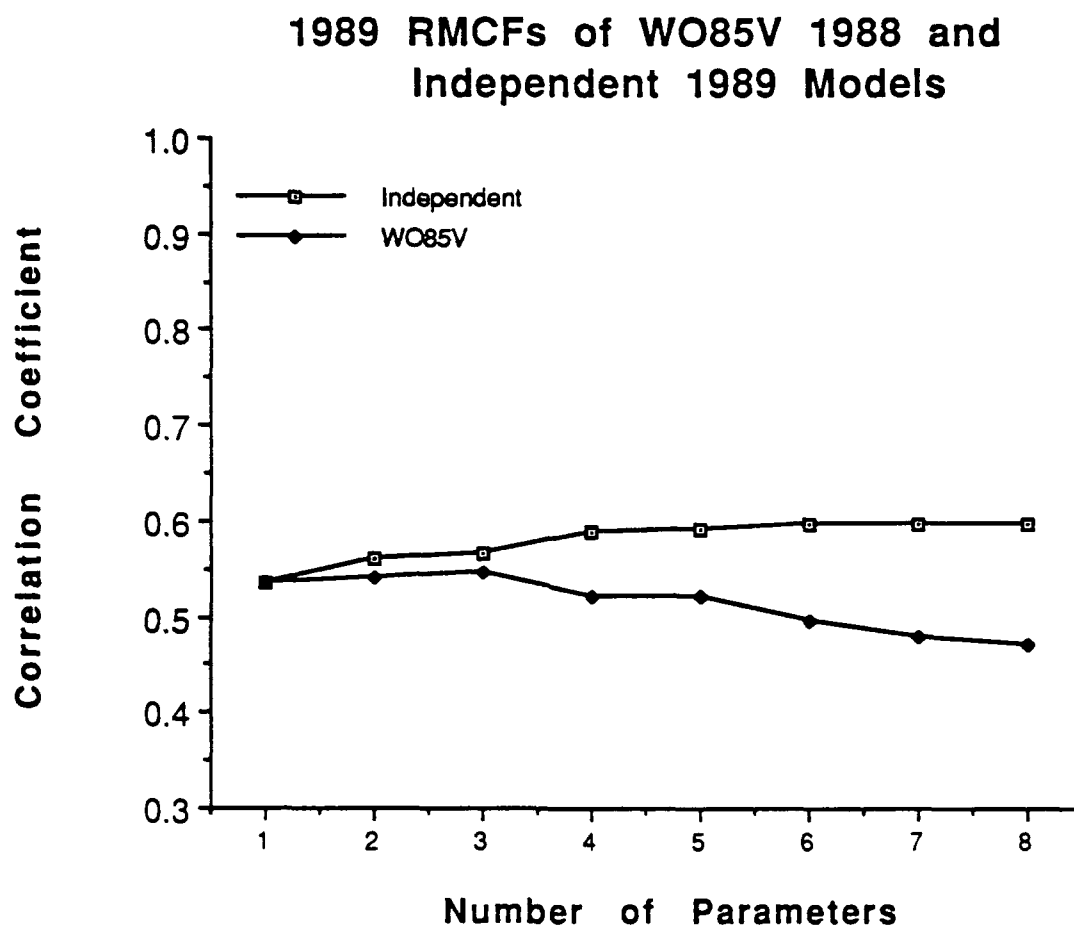


Figure 5.4: RMCFs of the WO85V 1988 microwave multi-parameter model applied to 1989 data and the independent 1989 multi-parameter model.

Table 5.4: Parameters used in independent 1989 regression model along with correlation coefficients.

Parameter	R
$37U_E$	-0.535
$85H_E$	-0.562
$19PCT_E$	-0.567
$19PCT_M$	-0.589
$37V_M$	-0.593
$22V_M$	-0.596
$37PCT_M$	-0.597
$85H_M$	-0.598



independent regression model, followed by  $85H_E$ ,  $19PCT_E$ , and  $19PCT_M$ . In 1988,  $37U_E$  again formed the basis of the optimal regression model, but is followed by  $22V_M$ ,  $19V_E$ , and  $85H_M$ . The parameters chosen in either year are based upon the parameter correlations with subdivisional rainfall and inter-correlations among individual parameters. In addition, the overlap process does occur as the number of parameters in the model increases. The entry of  $22V_M$  or  $19V_E$  into the models does not adversely affect the correlation, however the addition of  $85H_M$  does. At this point, the RMCF decreases to less than that of a single parameter model using  $37U_E$ .

The 1989 independent model, based upon different parameters, does show a steady rise in the correlation until reaching a limit of -0.605. This limit is significantly below that of optimal 1988 (-0.802) and is most likely related to the lack of useful 85V parameters which provides information concerning the amount of volume scattering present. However, the key physical radiative processes are accounted for in the 1989 independent model.

## CHAPTER 6

### Rainfall Accumulation

#### 6.1 Monsoon Features

To determine if basic monsoon features are observable using the optimal model applied to 1988 and 1987, and the WO85V model applied to 1989, the measured and model estimated rainfall and the difference between them were viewed in graphic format. Figure 6.1 shows this graphic for 1988. The rectangles contain these data for each subdivision on a weekly basis. The subdivisions were reordered by latitude (south at the top and north at the bottom of the rectangle) so that the progression of the monsoon could be easily observed. The time is plotted along the abscissa. The top rectangle contains the measured subdivisional rainfall data, the middle contains the model estimated rainfall data, and the bottom contains the difference between the measured and the model estimated rainfall data. The rainfall totals are color coded in 25 mm increments with grey representing bad data.

The progression of the monsoon is visible in the measured rainfall data as seen by the heavier rainfall totals propagating towards the north with time. A break period starts in the south at week 7 and also propagates north with time. This cycle is repeated until bad data is encountered which masks the behavior of the monsoon as represented by the measured rainfall. The same sequence is evident in the model estimated rainfall. In addition, the difference between the measured and estimated rainfall is less than 25

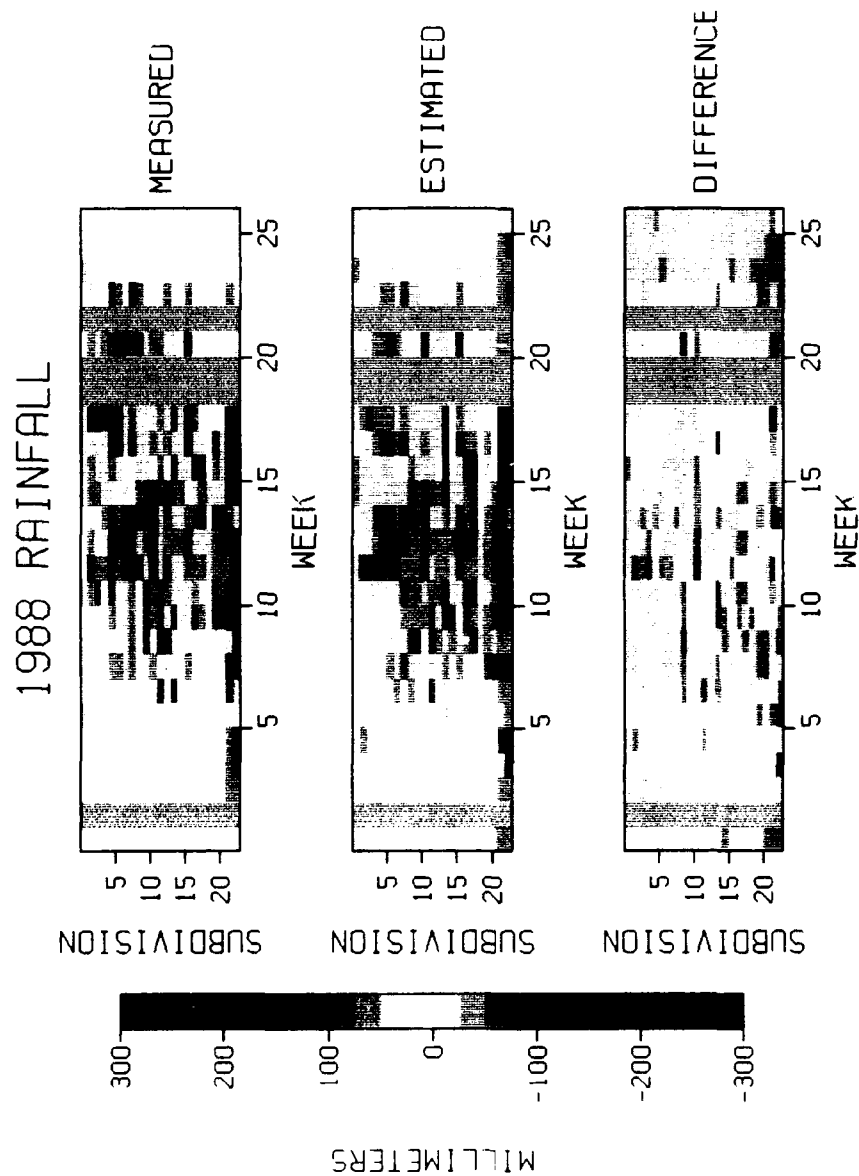


Figure 6.1: Measured and model estimated 1988 subdivisinal weekly rainfall and the difference between the measured and estimated data.

mm for the majority of the subdivisions.

Figure 6.2 shows the results of the optimal model applied to the 1987 data set. Again the active/break cycle is apparent in the measured data. In the model estimated data the cycle appears after week 5. During week 5, rainfall is greatly underestimated for all subdivisions and appears to be caused by bad data. With the exception of week 5, the majority of the differences are less than 25 mm.

Figure 6.3 shows the results of the WO85V model applied to the 1987 data set. The active/break cycle is less evident but observable by following the progression of the heavier rainfall totals of the measured rainfall data. The model estimated rainfall mimics the overall pattern but individual differences can be quite large as seen by the preponderance of brighter colors in the lower rectangle of Figure 6.3.

## 6.2 Space and Time Averages

**6.2.1 1988 accumulations.** Figure 6.4 contains the measured and model estimated continental weekly rainfall accumulations weighted by subdivision size for 1988. The average error is 62.8% but ranges from 0% to 380%. The first week and the last three weeks (weeks 1, 24, 25, and 26) exhibit the largest errors. These errors are most likely due to satellite sampling limitations. If these four weeks are eliminated, the average error drops to 12.2%. Thus on a weekly basis, the total accumulation calculated from the optimal model is in close agreement with the measured rainfall accumulations.

Figure 6.5 shows measured and model estimated subdivisional seasonal rainfall accumulations weighted by subdivision size. The average error is 20.28% and ranges from 0% in Assam and Meghalaya (area 3) to 46.7% in Bihar Plateau (area 8). Figure 6.6

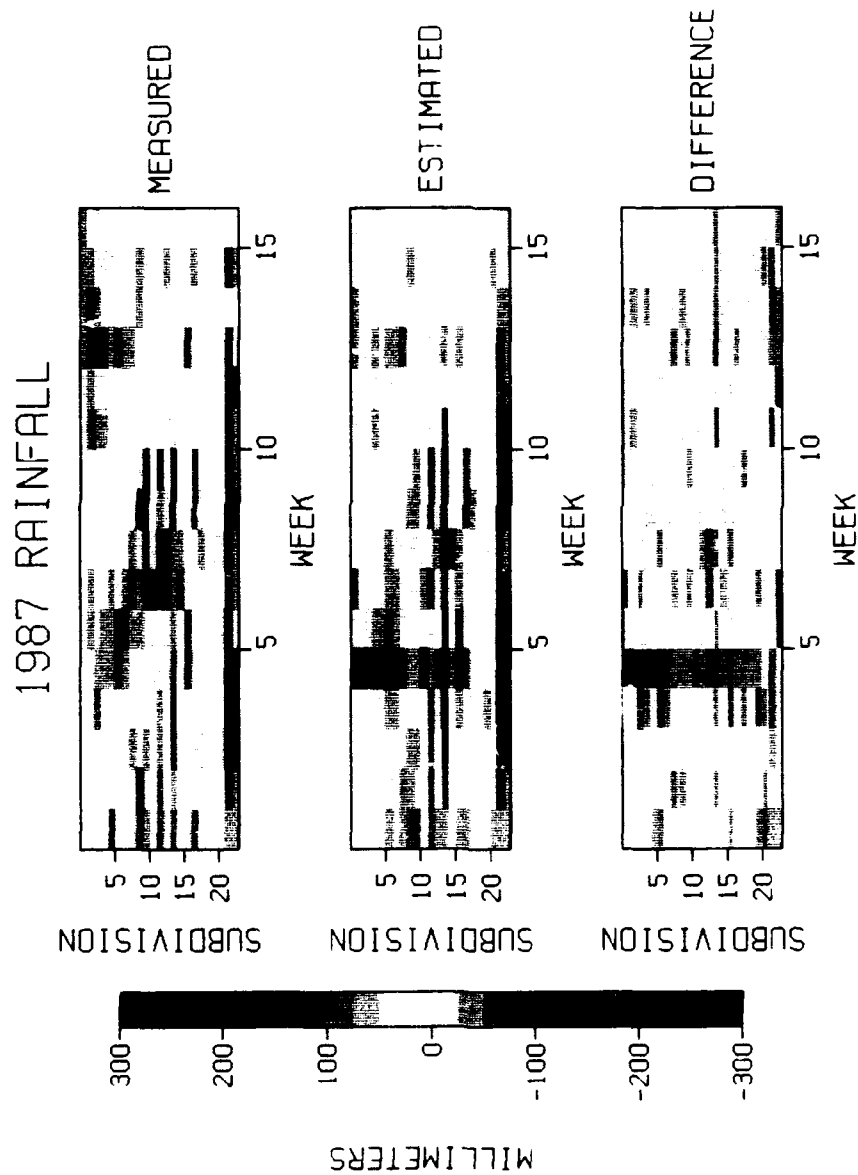


Figure 6.2: Measured and model estimated 1987 subdivisonal weekly rainfall and the difference between the measured and estimated data.

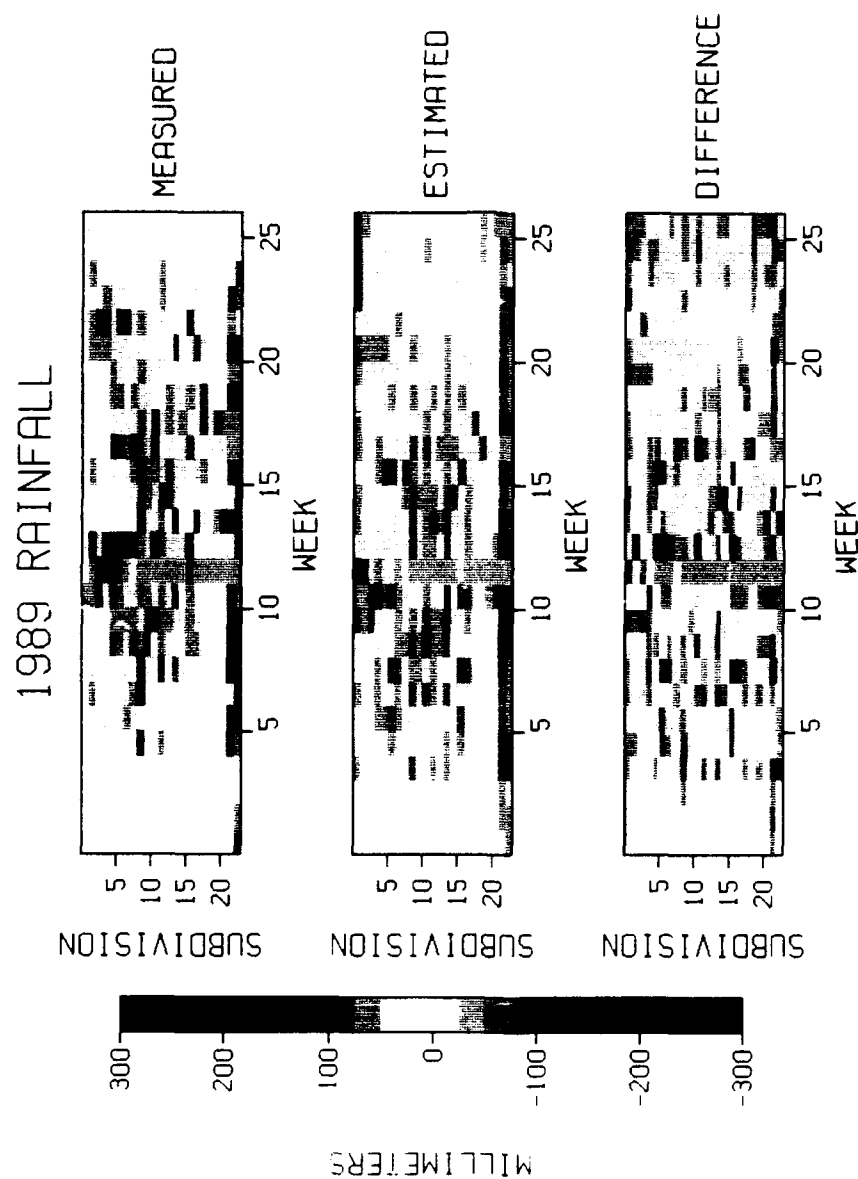


Figure 6.3: Measured and model estimated 1989 subdivisinal weekly rainfall and the difference between the measured and estimated data.

## Weighted Continental Weekly Rainfall 1988

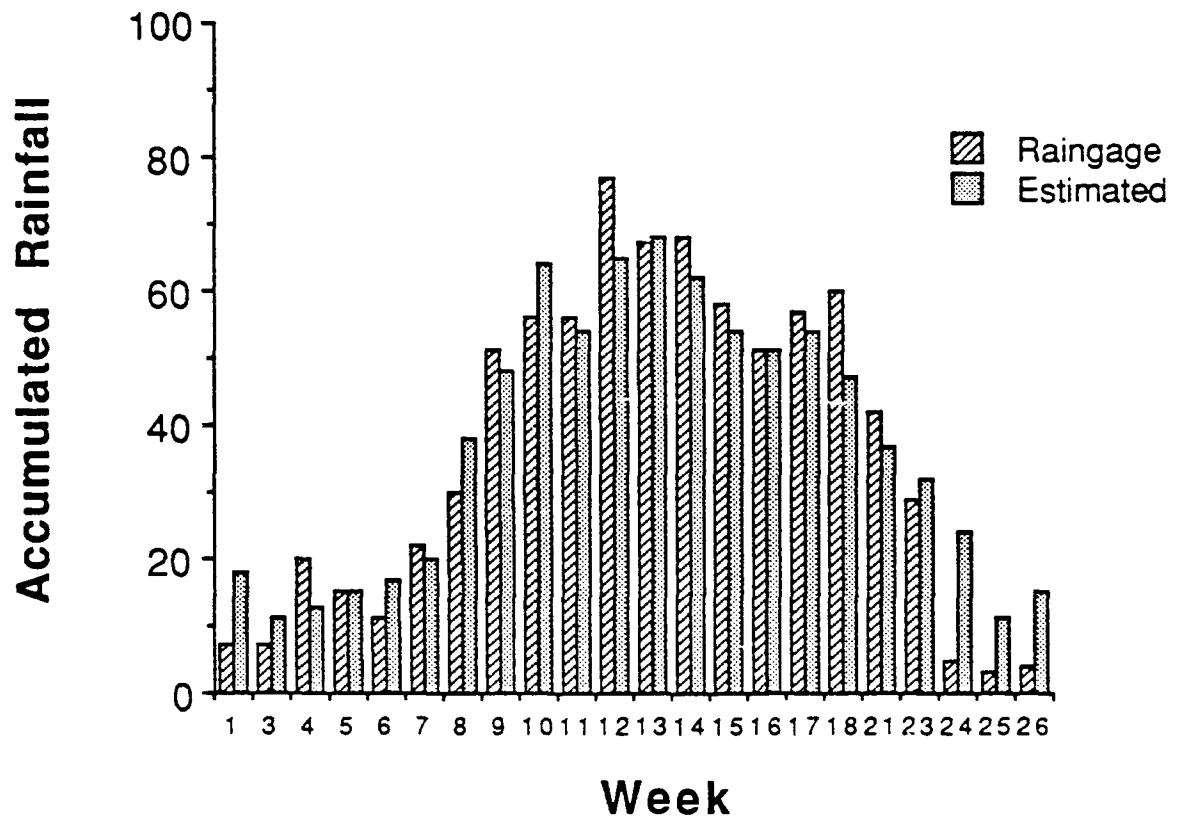


Figure 6.4: 1988 continental weekly rainfall accumulation weighted by subdivision size.

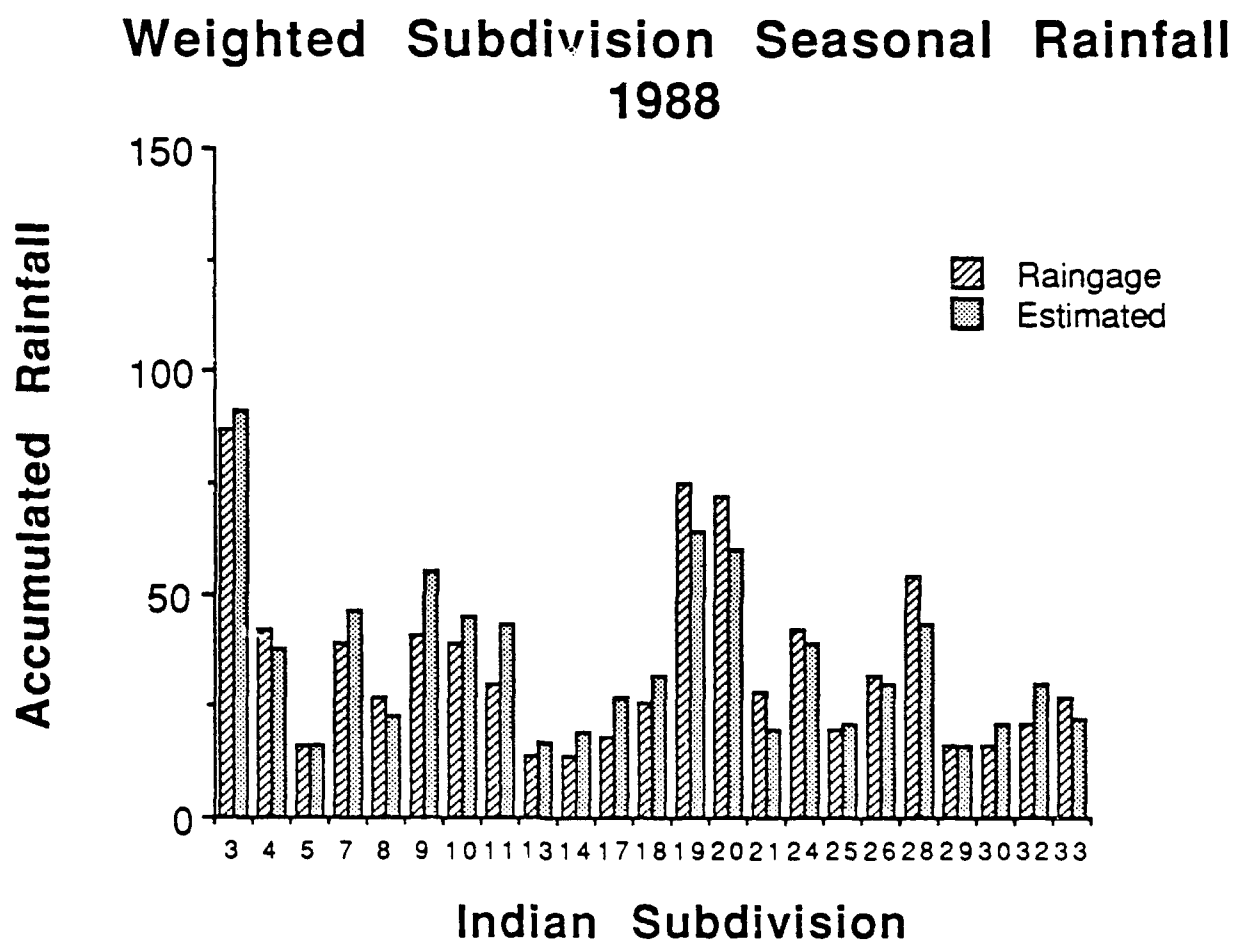


Figure 6.5: 1988 subdivisional seasonal rainfall accumulation weighted by subdivision size.



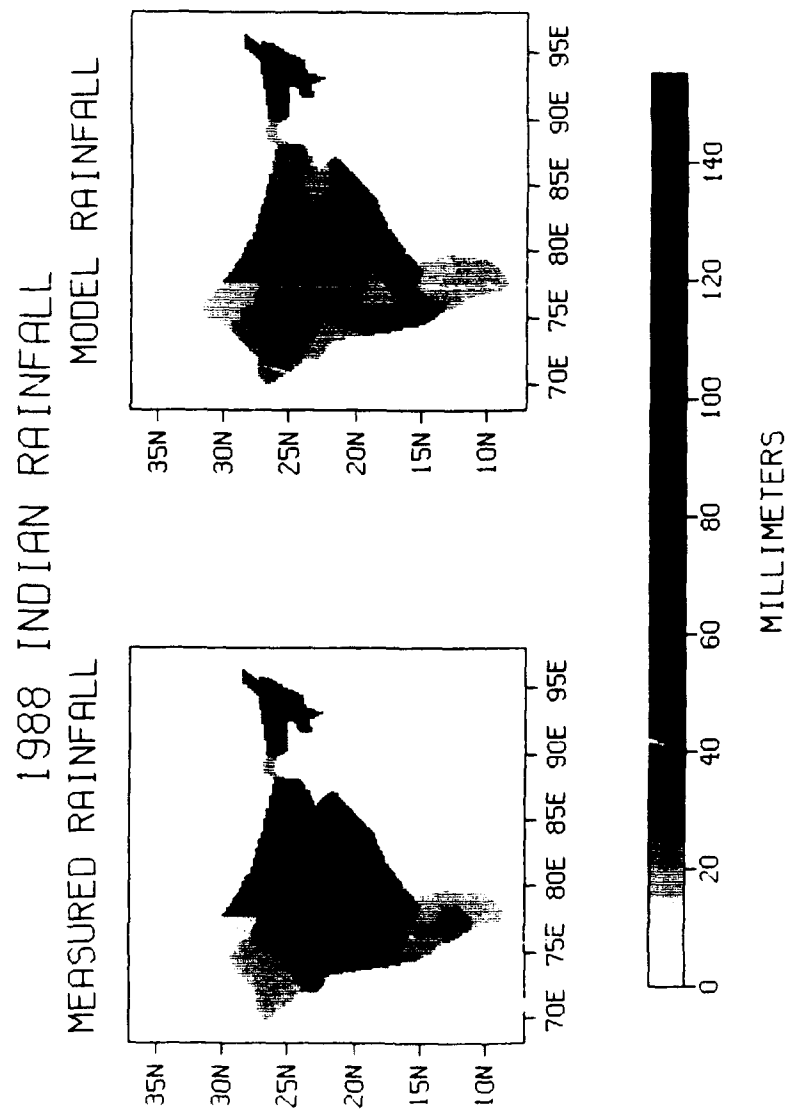


Figure 6.6: 1988 subdivisional seasonal rainfall accumulation map.

is a graphical representation of these data mapped to the appropriate Indian subdivision. As can be seen, the difference between the measured and estimated subdivisional seasonal rainfall accumulation is small.

**6.2.2 1987 accumulations.** Figure 6.7 contains the measured and model estimated continental weekly rainfall accumulations weighted by subdivision size for 1987. The average error is 34.79% but ranges from 0% to 125.6%. The fifth week exhibits the largest error and is probably due to the presence of bad data. Excluding this week, it appears that the model estimated continental weekly rainfall accumulation is a good approximation to the measured accumulations.

Figure 6.8 shows measured and model estimated subdivisional seasonal rainfall accumulations weighted by subdivision size. The average error is 34.93% and ranges 0% in Bihar Plateau (area 8) and the Gujarat region, Daman, Dadra and Nagar Haveli (area 21). Figure 6.9 is a graphical representation of these data mapped to the appropriate Indian subdivision. Again, the difference between the measured and estimated subdivisional seasonal rainfall accumulation is small. This is a consequence of the high correlation coefficient of the optimal model applied to the 1987 data set.

**6.2.3 1989 accumulations.** Figure 6.10 contains the measured and model estimated continental weekly rainfall accumulations weighted by subdivision size for 1989. The average error is 30.8% but ranges from 3% to 84.6%. Although this is the smallest average error of any of the three years, it is misleading because most of the individual errors are very close to the average error. In 1987 and 1988, most of the error was accounted for by a couple of events.

## Weighted Continental Weekly Rainfall 1987

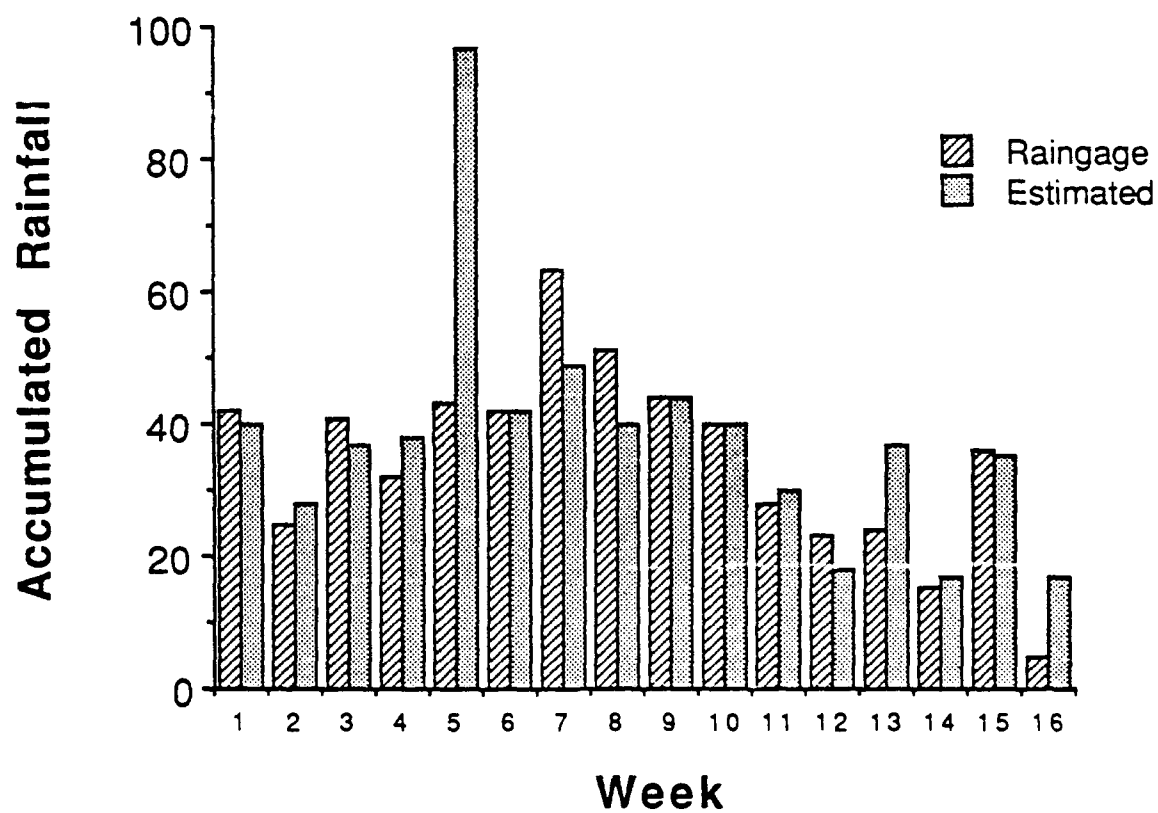


Figure 6.7: 1987 continental weekly rainfall accumulation weighted by subdivision size.

## Weighted Subdivision Seasonal Rainfall 1987

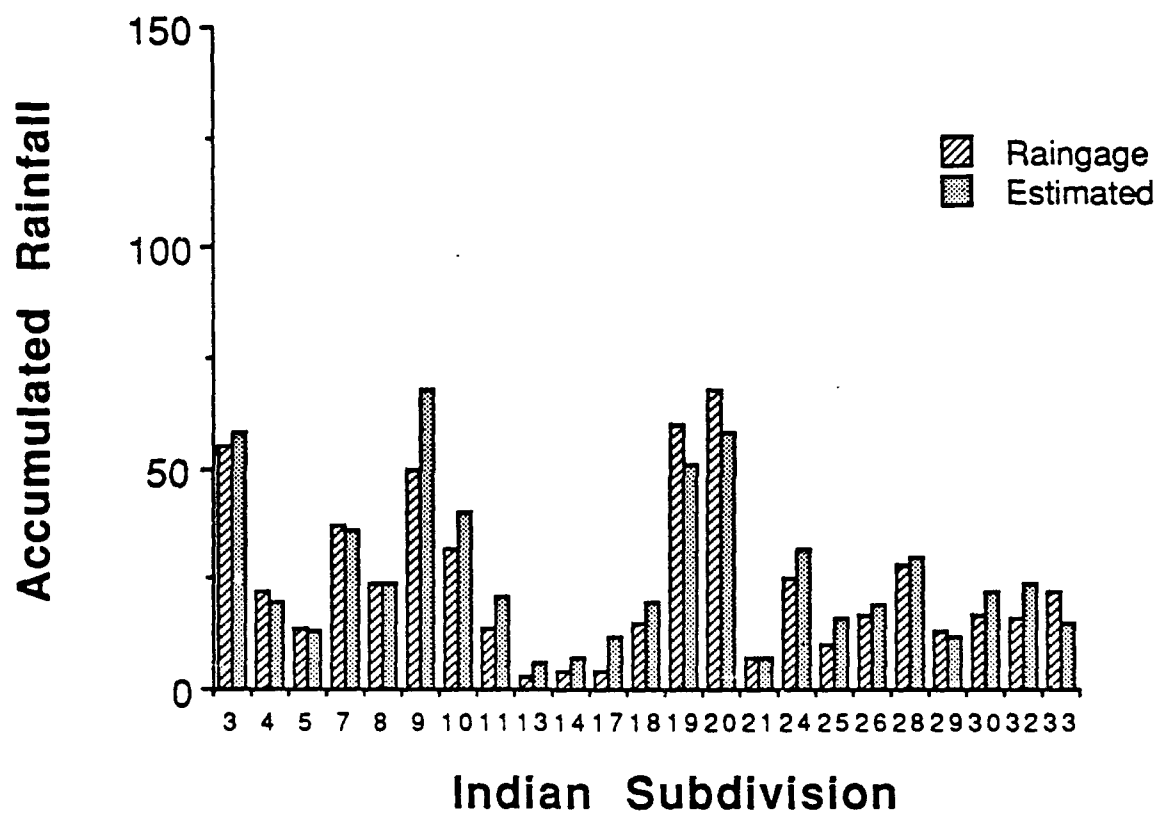


Figure 6.8: 1987 subdivisional seasonal rainfall accumulation weighted by subdivision size.

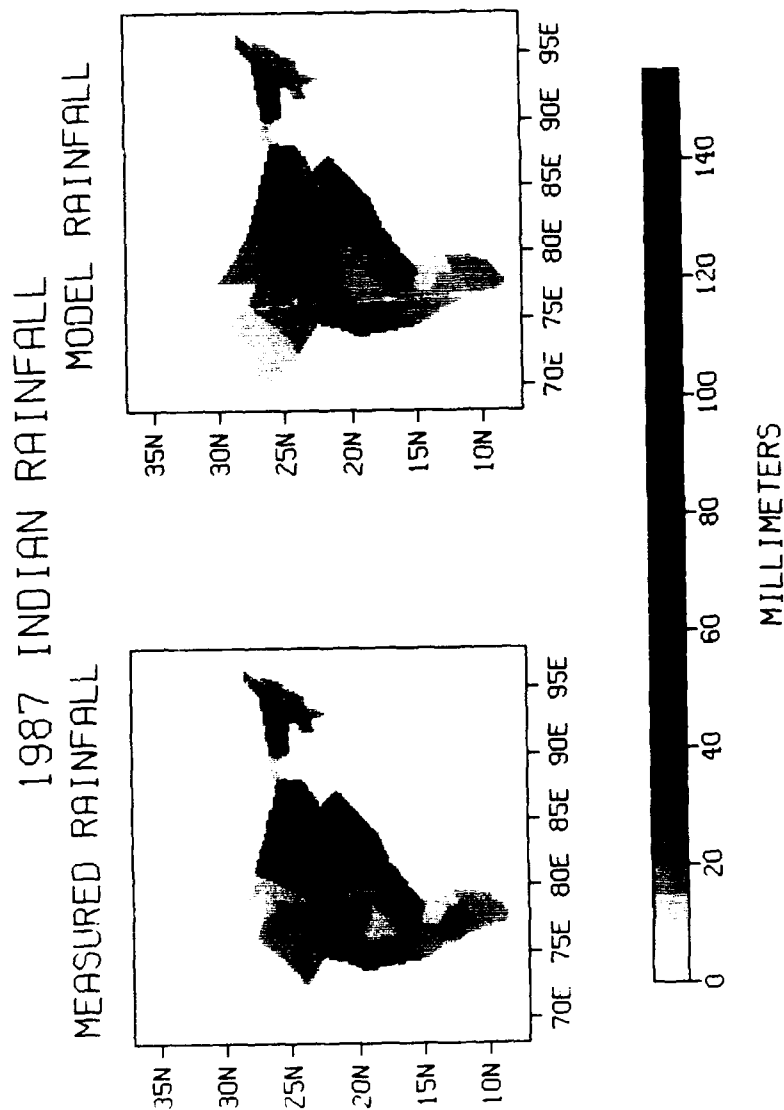


Figure 6.9: 1987 subdivisional seasonal rainfall accumulation map.

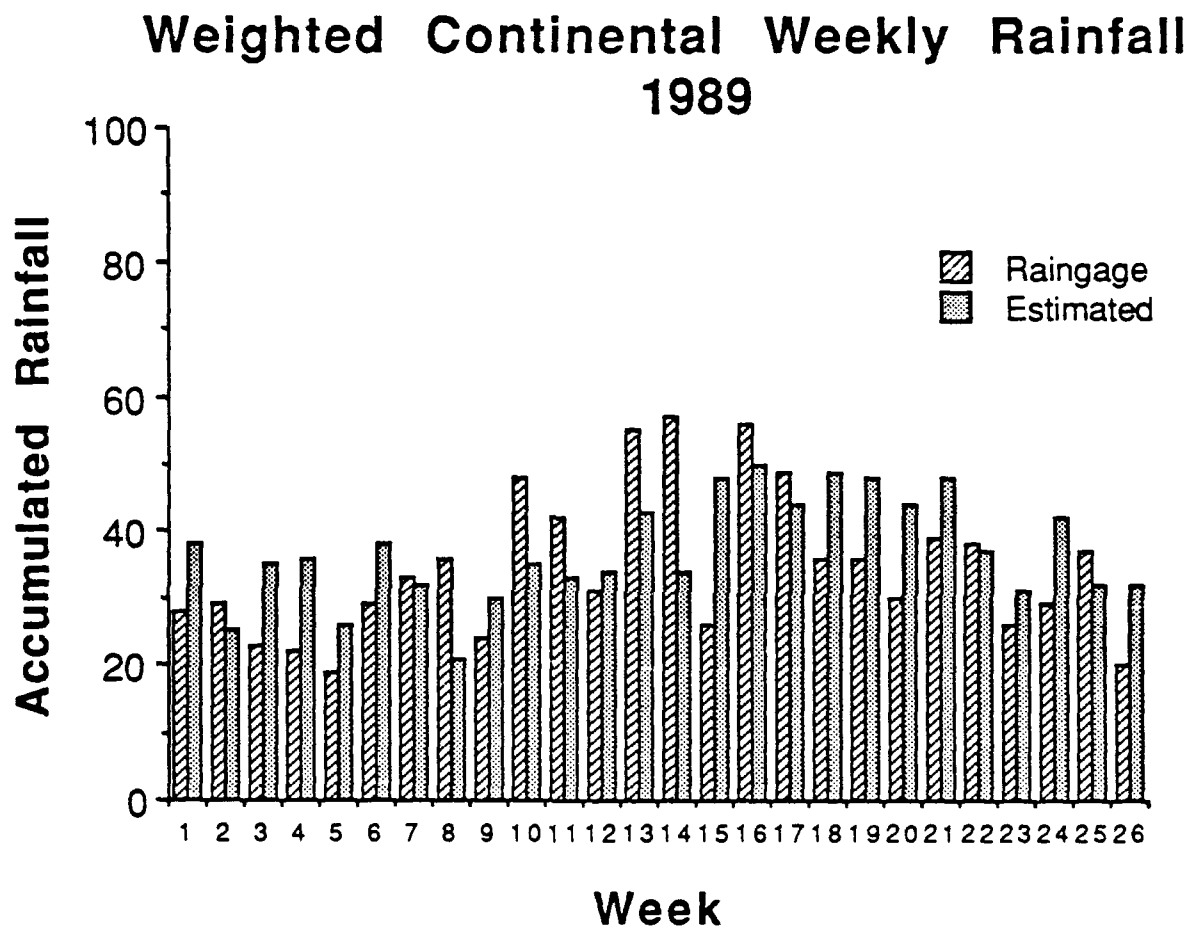


Figure 6.10: 1989 continental weekly rainfall accumulation weighted by subdivision size.

Figure 6.11 shows measured and model estimated subdivisional seasonal rainfall accumulations weighted by subdivision size. The average error is 68.75% and ranges 1.6% in East Uttar Pradesh (area 10) and 600% in South Interior Karnataka (area 33). These errors are related to the satellite sampling limitations and the limitations of the WO85V model applied to the 1989 data set. Figure 6.12 is a graphical representation of these data mapped to the appropriate Indian subdivision. During 1989, larger differences are discernable between the measured and estimated model subdivisional seasonal rainfall accumulations.

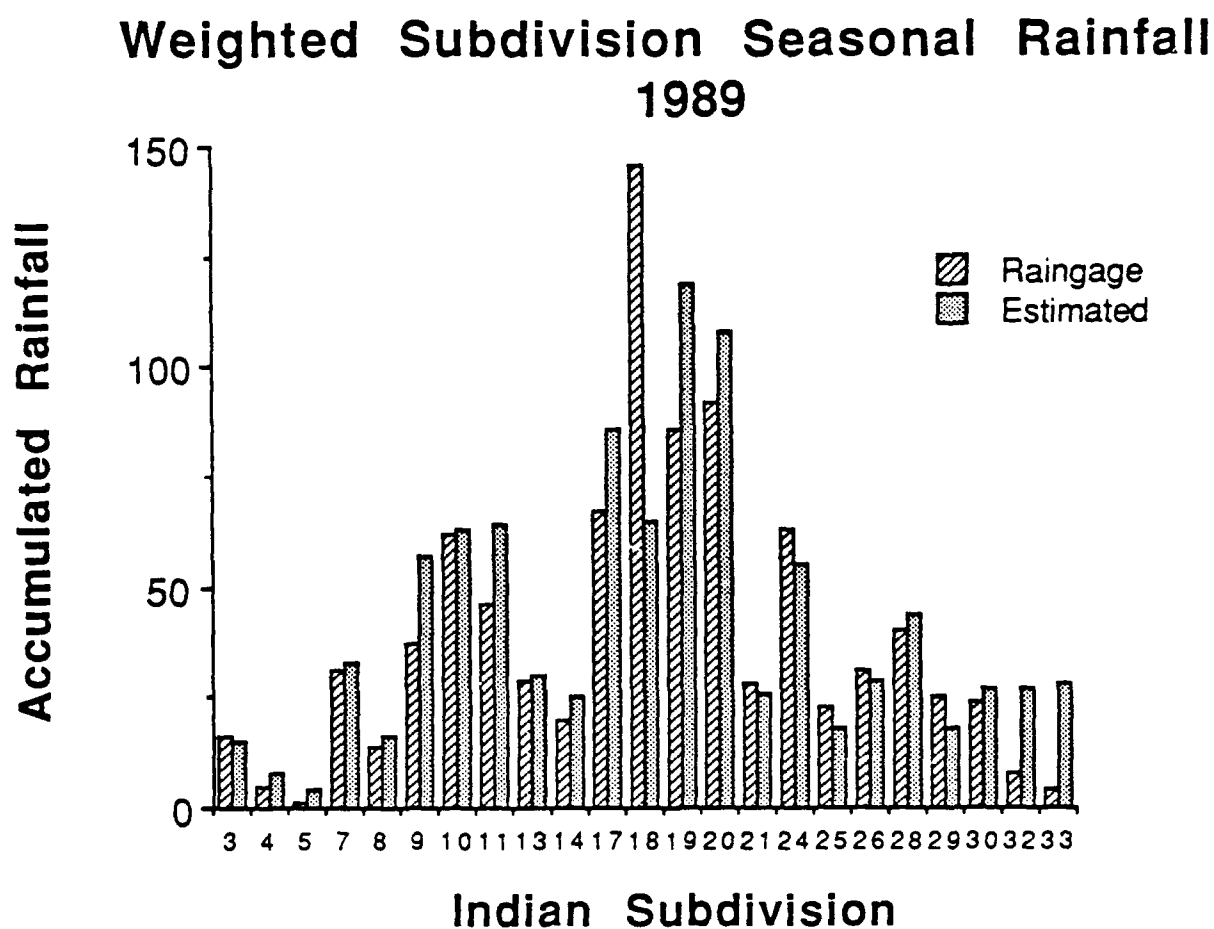


Figure 6.11: 1989 subdivisional seasonal rainfall accumulation weighted by subdivision size.



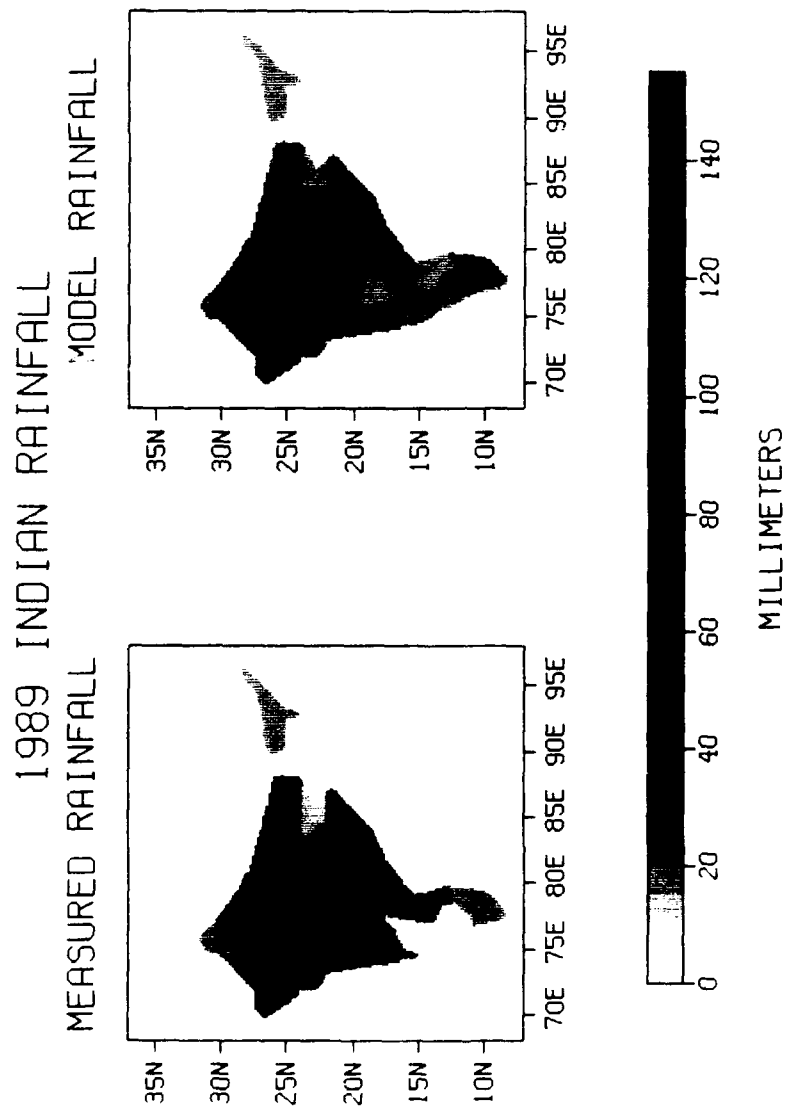


Figure 6.12: 1989 subdivisinal seasonal rainfall accumulation map.

## CHAPTER 7

### Summary and Conclusions

The retrieval of accurate rainfall measurements over land regions obtained through passive MW techniques is challenging due to the general lack of contrast between rainfall and the land background. Only when large ice particles are present above the rain layers are high contrasts assured. Ice causes strong volume scattering which is readily detectable at 37 and 85 GHz. Although the contrast between rain layers and the land surface is generally small, the emitted radiances from these two sources are caused by highly distinct radiative processes. Confronted with this situation, previous investigators have tried to separate rainfall from the land background. Until recently, investigators had to rely upon, low spatial resolution, low frequency measurements (6.6, 10.7, 18, 19 and 37 GHz) available from the ESMR-5, ESMR-6, and SMMR instruments. Beginning in 1987, a new class of instruments, the SSM/I, were launched aboard DMSP satellites. This instrument carries a four frequency, dual polarization (except 22 GHz), microwave sensor which represents the highest spatial resolution and frequency (85 GHz) ever flown on a satellite. The high spatial resolution of the 85 GHz channel and its sensitivity to volume scattering provides better contrast between rain and the land surface.

This study has been designed to determine how much contrast actually exists between raining and non-raining pixels for each of a large set of passive MW parameters. These parameters include, in addition to the seven channels of the SSM/I instrument, 12 combinations of these channels designed to take into account the frequency and polarization diversity. All of the parameters are composed of  $T_B$ s which have been deconvolved to the resolution of the 85 GHz channels. From the PDFs of these parameters, two variables are extracted; the mean and standard deviation. In addition, CDFs of the seven SSM/I channels are generated from the appropriate PDF by obtaining the cumulative count of  $T_B$ s within each  $T_B$  bin of the PDF. From the CDFs, two additional parameters are extracted; the slope and intercept factors. The slope factor is determined by measuring the gradient of  $T_B$  accumulation over the range of  $T_B$ s within the CDF of a Indian subdivision. The intercept factor is the coldest  $T_B$  present within the CDF.

This study utilizes the high rainfall variability on temporal and spatial scales available during the SW monsoon over India with which to evaluate the MW parameters. By calculating the correlation between the time-area averaged MW measurements in each Indian subdivision with it's weekly rainfall total, an evaluation of the robustness of each parameter is determined. In addition, INSAT IR measurements are utilized, to determine if their presence in an optimal multi-parameter regression model significantly improves microwave-only multi-parameter regression models.

The results reveal that the mean of the MW parameter measurements obtained during the evening have higher correlation coefficients than the same parameter correlations from the morning during 1988 and 1989. The opposite result was reached for the 1987 MW measurements. This difference may stem from the diurnal rainfall cycle and its inter-annual variability caused by large scale influences on the monsoon.

The MW parameters based upon the standard deviation, slope and intercept factors all have very low correlations with subdivisional rainfall and therefore cannot be considered robust variables.

Individually, the means of the  $37U_E$ ,  $19U_E$ ,  $19V_E$ ,  $19/22DIF_E$ ,  $37V_E$ ,  $19H_E$ ,  $22V_E$ , and  $37H_E$  PDFs are the most robust parameters in 1988 and 1989. During 1987, the most robust set of parameters were significantly different from 1988 and 1989 and are dominated by morning parameters. These parameters include the means of the  $85PCT_M$ ,  $85V_M$ ,  $19/22DIF_E$ ,  $85U_M$ ,  $19/22DIF_M$ ,  $37V_M$ ,  $37U_M$ , and  $19V_M$  PDFs. Only  $19/22DIF_M$  is common to all three years. These differences may be due to the differences in the rainfall characteristics of strong and weak monsoons. The means of the  $19NDP$ ,  $37NDP$ , and  $85NDP$  PDFs show little correlation with rainfall in any of the three years studied. The remainder of the parameters fall into an intermediate robustness class.

The optimal 1988 MW multi-parameter regression model reveals that a maximum correlation (-0.80) is reached after 8 parameters are added to the model. This multi-parameter approach leads to the conclusion that some individual parameters with relatively low correlations with measured rainfall provide important information concerning physical radiative processes when used in conjunction with other parameters. However, the overall performance of the optimal multi-parameter model is determined by the robustness of the first parameter in the model since it accounts for the majority of the explained variance.

The application of the optimal 1988 MW multi-parameter model on 1987 and the WO85V 1988 MW multi-parameter model on 1989 suggests that the magnitudes of the Regression Model Correlation Functions (RMCF) are smaller by 7.5% and 20% for 1987 and 1989, respectively than the independently derived regression models. In addition,

the behavior of the RMCs derived from the independent year multi-parameter regression models are also controlled by an 'overlap process'. The overlap process occurs when a class of parameters used in the independent 1987 and 1989 models are also contained in the optimal or WO85V 1988 models, respectively. Therefore, the implication of how parameters are selected for an optimal model is that key physical radiative processes (surface and rain-layer emission, within cloud volume scattering, water vapor variability, and polarization differences) must be accounted for. The overlap or combinations of parameters ensure that the key physical radiative processes are accounted for. This point must be qualified by the fact that 1989 lacked meaningful volume scattering parameters because the 85 GHz channels were missing or unreliable.

The inclusion of INSAT IR measurements into a optimal multi-parameter regression model does not substantially improve the performance obtained by pure MW models, however, fewer parameters are required to reach optimal performance. Individually, the mean of the morning IR PDFs are more robust than mean of any microwave parameter PDFs. However, the mean of the evening IR PDFs are less robust than the mean of morning IR PDFs and many MW parameter PDFs. This is probably caused by cirrus cloud contamination of FOVs generated by the anvils of large thunderstorms during the evening thunderstorm maximum in the diurnal cycle. The cirrus clouds creates very cold temperatures within the FOV which are not related to rainfall. In addition, a pronounced diurnal cycle is evident between the robustness and the time of the satellite measurements.

## References

- Choudhury, B.J., 1989: Monitoring global land surface using Nimbus-7 37 GHz data. Theory and Examples. *Int. J. Remote Sensing*, 10, 1579-1605.
- Das, N., D.S. Desai, and N.C. Biswas, 1989: Monsoon season (June - September 1988). *Mausam*, 40, 351-364.
- Durkee, P.A., 1980: Summer precipitation frequency of the north central U.S. from satellite microwave observations. Master's Degree Thesis, Colorado State University.
- Farrar, M.R., 1991: Spatial resolution enhancement of SSM/I microwave brightness temperatures and its impact on rainfall retrieval algorithms. Master's Degree Thesis, Florida State University.
- Gupta, G.R., D.S. Desai, and N.C. Biswas, 1990: Monsoon season (June - September 1989). *Mausam*, 41, 505-520.
- Hinton B.B., W.S. Olson, D.W. Martin, and B. Auvine, 1992: A passive microwave algorithm for tropical oceanic rainfall. Submitted to *J. Appl. Meteor.*
- IMSL, 1989: FORTRAN subroutines for statistical analysis, version 1.1.
- Lamm, J.E., E.A. Smith, A.V. Mehta, and R. Jenne, 1991: Description of the U.S. INSAT satellite data set (April 1984 to April 1989).
- Montgomery, D.C., and E.A. Peck, 1982: *Introduction to Linear Regression Analysis*, John Wiley and Sons, 504 pp.
- Olson, W.S., C.-L. Yeh, J.A. Weinman, T.T.Chin, 1986: Resolution enhancement of multichannel microwave imagery from the Nimbus-7 SMMR for maritime rainfall analysis. *J. Atmos. Oceanic Tech.* 3, 422-432.
- Ramage, C.S., 1971: *Monsoon Meteorology*. Academic Press, 296pp.

Robinson, W.D., C. Kummerow, W.S. Olson, 1991: A technique for enhancing and matching the resolution of microwave measurements from the SSM/I instrument.

Rodgers, E., and H. Siddalingaiah, 1983: The utilization of Nimbus-7 measurements to delineate rainfall over land. *J. Clim. Appl. Meteorol.*, **22**, 1753-1763.

Savage, R.C., and J.A. Weinman, 1975: Preliminary calculations of the upwelling radiance from rainclouds at 37.0 and 19.35 GHz. *Bull. Am. Meteorol. Soc.*, **56**, 1272-1274.

Schmugge, T.J., 1983: Remote sensing of soil moisture: Recent advances. *IEEE Trans. Geosci. Remote Sens.*, **GE21**, 336-344.

Shin, K.-S., P.E. Riba, and G.R. North, 1990: Estimation of area-averaged rainfall over tropical oceans from microwave radiometry: A single channel approach. *J. Appl. Meteorol.*, **29**, 1031-1042.

Sivaramakrishnan, T.R., 1990: An analytical study of thunderstorms over Sriharikota. *Mausam*, **41**, 489-491.

Smith, E.A., S.Q. Kidder, 1978: A multispectral satellite approach to rainfall estimates. Presented at the 18th AMS Conf. on Radar Meteorology (28-31 March; Atlanta GA); for summary, see E.C Barrett and D.W. Martin, *The Use of Satellite Data in Rainfall Monitoring*, Academic Press, 160-163.

Smith, E.A. and A. Mugnai, 1988: Radiative transfer to space through a precipitating cloud at multiple microwave frequencies. Part II: Results and analysis. *J. Appl. Meteorol.*, **27**, 1074-1091.

Smith, E.A., M.R. Farrar, and A. Mugnai, 1991: Spatial resolution enhancement of 19 and 37 GHz SSM/I brightness temperatures. Presented at the WetNet Science and Analysis Colloquium (19-22 February, 1991; University of California - Santa Barbara).

Spencer, R.W., 1984: Satellite passive microwave rain rate measurements over croplands during spring, summer, and fall. *J. Clim. Appl. Meteorol.*, **23**, 1553-1562.

Spencer, R.W., and D.A. Santek, 1985: Measuring the global distribution of intense convection over land with passive microwave radiometry. *J. Clim. Appl. Meteorol.*, **24**, 860-864.

Spencer, R.W., H.M. Goodman, R.E. Hood, 1989: Precipitation retrieval over land and ocean with the SSM/I: Identification and characteristics of the scattering signal. *J. Atmos. Oceanic Tech.*, **6**, 254-273.

Weinman, J.A., and P.J. Guetter, 1977: Determination of rainfall distributions from microwave radiation measured by the Nimbus-6 ESMR. *J. Appl. Meteor.*, **16**, 437-442.

Wentz, F.J., 1991: User's Manual. SSM/I antenna temperature tapes. Revision 1, RSS Tech Rpt. 120191, 70 pp, Remote Sensing Systems, Santa Rosa, CA.

Wilheit, T.T., 1972: The electrically scanning microwave radiometer (ESMR) experiment. *Nimbus 5 Users Guide*, NASA Goddard Space Flight Center, 55-105.

Wilheit, T.T., A.T.C. Chang, M.S.V. Rao, E.B. Rodgers and J.S. Theon, 1977: A satellite technique for quantitatively mapping rainfall rates over the ocean. *J. Appl. Meteor.*, **16**, 551-560.

Wilheit, T.T., and A.T.C. Chang, 1991: Retrieval of monthly rainfall indices from microwave radiometric measurements using probability distribution functions. *J. Atmos. Oceanic Tech.*, **8**, 118-136.



## BIOGRAPHICAL SKETCH

John Shattuck was born in Highland Park, MI on May 8, 1957. He enlisted in the U.S. Air Force in 1976 and was assigned to Ft. Stewart, GA as a weather observer. He was selected in 1978 to participate in the First GARP (Global Atmospheric Research Program) Global Experiment (FGGE) as a dropwindsonde systems operator aboard WC-135 and C-141 aircraft. Following FGGE, he was assigned to the 54th Weather Reconnaissance Squadron, Andersen AFB, Guam, where he served as a dropsonde systems operator aboard WC-130 aircraft.

Upon leaving the Air Force in 1980, John Shattuck then enrolled at the University of Wisconsin - Oshkosh and transferred to the University of Wisconsin - Madison where he received a B.S. in Meteorology in December 1985. Following graduation, John Shattuck attended Officer Training School at Lackland AFB, TX and was subsequently commissioned as a 2Lt in the U.S. Air Force during June 1986. He was then assigned to Hickam AFB, HI and held the positions of forecaster, command briefer, and Meteorological Satellite (METSAT) Coordinator. While in Hawaii, John Shattuck attended Chaminade University of Honolulu to pursue a Master's degree in Business Administration.

Upon his return to the mainland, John Shattuck then enrolled at Florida State University in order to pursue a Master's degree in Meteorology under Dr. Eric Smith, his major professor. John Shattuck currently holds the rank of

Captain, and will serve as the METSAT Coordinator at the Joint Typhoon Warning Center (JTWC), Nimitz Hill, Guam, following his graduation in August 1992.